Structural neural connectivity analysis in zebrafish with restricted anterograde transneuronal viral labeling and quantitative brain mapping

Manxiu Ma[1,2,#], Stanislav Kler[1,2,#], and Y. Albert Pan[1,2,3*]

[1]Center for Neurobiology Research, Fralin Biomedical Research Institute at VTC, Virginia Tech, Roanoke, VA.

[2]Department of Neuroscience and Regenerative Medicine, Medical College of Georgia, Augusta University, Augusta, GA.

[3]Department of Biomedical Sciences and Pathobiology, Virginia-Maryland College of Veterinary Medicine, Virginia Tech, Blacksburg, VA.

[#]Equal contributions.

*Correspondence should be addressed to Y. Albert Pan yapan@vtc.vt.edu

Conflict of Interest

The authors declare no conflict of interest.

Acknowledgments

This work was supported by funding from the National Institutes of Health (R01 EY024844 to Y.A.P.), Augusta University, and Virginia Tech. We thank the animal care staff at Augusta University

and Virginia Tech for animal husbandry, Owen Randlett for help with Z-Brain analysis, Didem Gotz Ayturk, Xiang Ma, and Constance Cepko for reagents and technical expertise for virus preparation, and members of the Pan lab for helpful suggestions on the manuscript.

Abstract

The unique combination of small size, translucency, and powerful genetic tools makes larval zebrafish a uniquely useful vertebrate system to investigate normal and pathological brain structure and function. While functional connectivity can now be assessed (via fluorescent calcium or voltage reporters) at the whole-brain scale, it remains challenging to systematically determine structural connections and identify connectivity changes during development or disease. To address this, we developed Tracer with Restricted Anterograde Spread (TRAS), a novel vesicular stomatitis virus (VSV)-based neural circuit labeling approach. TRAS makes use of replication-incompetent VSV (VSVΔG) and a helper virus (lentivirus) to enable anterograde transneuronal spread between efferent axons and their direct postsynaptic targets but restricts further spread to downstream areas. We integrated TRAS with the Z-Brain zebrafish 3D atlas for quantitative connectivity analysis and identified targets of the retinal and habenular efferent projections, in patterns consistent with previous reports. We compared retinofugal connectivity patterns between wild-type and *down syndrome cell adhesion molecule-like 1* (*dscaml1*) mutant zebrafish and revealed differences in topographical distribution and potential changes in the retinofugal targeting of excitatory versus inhibitory retinorecipient cells. These results demonstrate the utility of TRAS for quantitative structural connectivity analysis that would be valuable for detecting novel efferent targets and mapping connectivity changes underlying neurological or behavioral deficits.

Introduction

The function of the brain is closely linked to its structure, how its billions of constituent cells are wired and connected by trillions of synapses. Understanding how these connections are formed and maintained is key to gaining mechanistic insight towards brain function and identifying the causes and treatments for neuropsychiatric disorders (Belmonte et al., 2004; Lynall et al., 2010; Fornito et al., 2015). Techniques for mapping the structure and function of the brain have progressed rapidly in past decades, from anatomical structural analysis to functional computation, and from human participants to animal models (Kasthuri et al., 2015; Glasser et al., 2016). However, the large number of neurons and vast spatial scale of neuronal structures (from meters to nanometers) of the mammalian brain makes mapping neuronal networks at the cellular level and correlating them with development and disease a daunting task (Swanson and Lichtman, 2016).

Zebrafish (*Danio rerio*), a small tropical fish, has emerged as an accessible model for studying behavior, neuronal networks, and cellular connectivity (Orger and de Polavieja, 2017). Zebrafish has analogous neuroanatomy and neurochemistry to mammals and can perform complex sensory, motor, and cognitive functions early during larval stages (5-10 days post fertilization, dpf). Importantly, at this stage, there are only roughly 100,000 neurons in the brain, 80% of which can be imaged and physiologically recorded in live, behaving animals (Ahrens et al., 2013; Chen et al., 2018; Abdelfattah et al., 2019). As a result, zebrafish whole-brain functional imaging studies have been able to generate cellular resolution neuronal activity maps under

different behavioral contexts and linking activity maps to disease states such as autism spectrum disorder and epilepsy (Sakai et al., 2018; Thyme et al., 2019). The ability to fully interpret patterns of functional connectivity and determine causality for disorders, however, is limited by the lack of detailed structural information on neuronal wiring in zebrafish, which still lags behind other commonly used model organisms like mice, *Drosophila*, and *C. elegans*. Efforts are ongoing to map the full complement of neuronal connections (i.e., connectome) with electron microscopy in the larval and adult zebrafish, but the time and labor-intensive nature of synapse-level reconstruction has thus far restricted investigations to connections within smaller brain regions (Wanner et al., 2016; Hildebrand et al., 2017; Vishwanathan et al., 2017; Svara et al., 2018).

To address this, we sought to develop a virus and light imaging-based structural mapping technique that would allow for quantitative brain-wide mapping of neuronal connectivity in larval zebrafish. Previously, we found that recombinant vesicular stomatitis virus (VSV) can function as an anterograde transsynaptic tracer in a wide range of organisms (Mundell et al., 2015). VSV is a negative-strand RNA virus in the *Rhabdoviridae* family, which also includes the rabies virus (RABV). In contrast to RABV, which spreads retrogradely (from dendrite to presynaptic afferent axons), VSV spreads anterogradely (from efferent axons to their postsynaptic targets) when enveloped by its endogenous glycoprotein (VSV-G) (Beier et al., 2011b; Mundell et al., 2015). VSV injection into the retina of mice, chicken, and larval zebrafish lead to highly efficient labeling of the optic nerve and targets of the visual pathway, including both direct retinorecipient connections and areas further downstream. These findings open the door for utilizing VSV for zebrafish structural circuit mapping. Substantial limitations, however, still remain. First, the spread of VSV is

unrestricted, making it difficult to disambiguate direct (monosynaptic) and indirect (polysynaptic) connections. Second, replication-competent VSV and VSV-G expression are cytotoxic and lead to rapid deterioration of health in larval zebrafish (Hoffmann et al., 2010; Mundell et al., 2015). Finally, there is no established method for quantifying and annotating viral labeling in zebrafish, which is necessary to correlate anatomical tracing with functional imaging.

In this study, we developed a novel approach utilizing replication-incompetent VSV to achieve restricted anterograde transneuronal spread in zebrafish. We also developed an imaging and processing pipeline to register 3D image stacks to the widely used and extensively annotated Z-Brain digital atlas (Randlett et al., 2015). This method, termed TRAS (Tracer with Restricted Anterograde Spread), allows for a quantitative description of efferent connectivity based on neurotransmitter types and specific locations. We applied TRAS to investigate the axon projection patterns of retinorecipient cells and identified potential connectivity changes in zebrafish carrying a mutation in *down syndrome cell adhesion molecule-like 1 (dscaml1)*, a causal gene for autism spectrum disorder and human cortical abnormalities (Fuerst et al., 2009; Iossifov et al., 2014; Karaca et al., 2015; Galicia et al., 2018; Ma et al., 2019).

Materials and Methods

Zebrafish husbandry

Zebrafish (all ages) were raised under a 14/10 light/dark cycle at 28.5°C. Embryos and larvae were raised in water containing 0.1% Methylene Blue hydrate (Sigma-Aldrich). With the

exception of *nacre* mutants, embryos were transferred to E3 buffer containing 0.003% 1-phenyl-2-thiourea (PTU; Sigma-Aldrich) to prevent pigment formation at 24 hours post-fertilization. Developmental stages are as described by Kimmel et al. (Kimmel et al., 1995). Sex was not considered as a relevant variable for this study, as laboratory zebrafish remain sexually undifferentiated until two weeks of age, beyond the stages being used (0-9 dpf) (Maack and Segner, 2003; Wilson et al., 2014). All experimental procedures are performed in accordance with Institutional Animal Care and Use Committee guidelines at Augusta University and Virginia Tech.

Transgenic and mutant zebrafish lines

The *dscaml1*^{vt1} mutant line was generated by TALEN-targeted mutagenesis, which resulted in a seven base pair deletion and subsequent early translational termination (Ma et al., 2019). The *Tg(elavl3:H2B-GCaMP6f)* line was generously provided by E. Aksay at Weill Medical College, with permission from M. Ahrens at HHMI Janelia Farm Research Campus (Kawashima et al., 2016). The *vglut2a:GFP* line [*Tg(slc17a6b:EGFP)*] was generously provided by J. Fetcho at Cornell University with permission from S. Higashijima at the National Institute for Basic Biology (Bae et al., 2009).

Preparation of VSVΔG

VSV was prepared using methods detailed by Beier et al. 2016 (Beier et al., 2016). 293T cells (ATCC, #CRL-3216) were transfected at 80% confluency on 75 cm^2 flasks with 7 μg of *pCI-VSVG* plasmid (Addgene, #1733) and incubated overnight at 37°C. Afterward, cells were infected with VSVΔG-RFP (VSVΔG for short) (Beier et al., 2011b) at a multiplicity of infection (m.o.i.) of 0.1.

Viral supernatants were collected for the subsequent three days at 24-hour intervals and combined. Cell debris was precipitated by centrifugation at 1,000 g for 20 min. To concentrate VSVΔG, viral supernatant was ultracentrifuged for three hours at 80,000 g with an SW32Ti rotor, and the pellet was resuspended in 100 μl of culture medium. Viral stocks were titered by serial dilution on 90% confluent 293T cells. The number of fluorescent foci was calculated at two days post infection (dpi) by identifying RFP-positive cells. Typical viral titer was higher than $1x10^9$ focus forming units/ml (ffu/ml).

For *in vitro* trans-complementation of VSVΔG with lentivirus, BHK-21 cells (ATCC, #CCL-10) were seeded into 96-well plate and incubated overnight to reach 20,000 cells per well. Cell culture was co-infected with VSVΔG (m.o.i.=0.005) and VSV-G pseudotyped lentivirus (m.o.i.=0-10,000) (lentivirus-SIN-CMV-eGFP or lentivirus-SIN-Ubi-iCre-mCherry; GT3 Core Facility of the Salk Institute). At two hours post infection, cells were washed twice with PBS and incubated with fresh medium supplemented with 2% serum. At 2 dpi, the spread of VSV was visualized by fluorescent microscopy. The media in each well were collected and titered to evaluate viral yield.

Virus injection

Viral injections were performed as previously described (Mundell et al., 2015; Beier et al., 2016). Briefly, glass capillaries (TW100F-4; World Precision Instruments) were pulled into injection needles with a pipette puller (P-97; Sutter Instruments). The tips of injection needles were trimmed to create a ~10 μm opening. Virus injection solution was made by diluting VSVΔG and lentivirus stock with tissue culture medium (DMEM; Fisher Scientific), with Fast Green dye

(BP123-10; Fisher Scientific) as the injection marker. 2 μl of injection solution was loaded into the injection needle with a Microloader pipette tip (930001007; Eppendorf), and mounted into a microelectrode holder connected to a pneumatic PicoPump (PV820; World Precision Instruments). Injection volume was determined by calibrating the volume of the injected droplet on a stage micrometer (50-753-2911; Fisher Scientific). The hold pressure of the PicoPump was adjusted so that there was a slight outflow of virus solution when the needle tip was immersed in fish water.

For retina injection, 2.5 or 3 dpf larvae were anesthetized in Tricaine (0.013% w/v, AC118000500; Fisher Scientific) mounted laterally inside the center chamber of a glass-bottom dish (P50G-1.5-14-F; MatTek) with 1.5% low melting-point agarose (BP1360; Fisher Scientific). After the agarose has solidified, the dish is filled with Tricaine solution (0.013%) to maintain anesthesia. Under a stereo dissecting microscope (SMZ18; Nikon), the needle tip was moved with a micromanipulator (MN-151; Narishige) to approach the fish from the rear and penetrated the temporal retina, with the needle tip being in the neural retina. 0.25-0.5 nl of virus solution (concentrations as described in the Results section) were injected inside the retina. After injection, larvae were recovered from the agarose and returned to a 28°C incubator. Overall, the combination of VSVΔG and lentivirus (i.e., TRAS) only labeled cells in areas innervated by or adjacent to the optic nerve. It is worth noting that in one experiment we did observe neuronal cell bodies in the hindbrain and contralateral midbrain, which are two synapses downstream from RGCs (Helmbrecht et al., 2018) (1-2 cells in 50% of injected fish, n=10, Supplementary Figure S1). This may be due to VSVΔG self complementation in the retinorecipient cells at high m.o.i.

For all quantitative analysis involving selective labeling for primary retinorecipient cells, we used viral titers that did not result in secondary spread (VSVΔG at $3x10^7$ ffu/ml and lentivirus at $3x10^{10}$ ffu/ml).

For habenula injection, 3 dpf larvae were mounted as described for retina injection, with the dorsal side up. The agarose and skin above the left habenula were carefully removed with a sharpened tungsten needle (10130-05; Fine Science Tools). The injection needle tip was inserted into the left habenula and remained there for 5 s, allowing the slow outflow of virus solution (VSVΔG at $3x10^8$ ffu/ml, lentivirus at $1x10^{11}$ ffu/ml) to immerse the surrounding tissue. At 1 dpi, larvae with habenula-specific RFP expression were screened and later fixed at 3 dpi for immunohistochemistry and confocal imaging.

Immunohistochemistry

Whole-mount immunohistochemistry was performed as described by Randlett et al. 2015 (Randlett et al., 2015). Zebrafish larvae were fixed overnight with 4% PFA and 0. 25% Triton X-100 (Fisher Scientific) in 1X PBS (diluted from 10%PFA; Polysciences), then washed with 1X PBS and 0. 25% Triton X-100. H2B-GCaM6f was stained with FluoTag-X4 anti-GFP (N0304-At488; NanoTag); GABA was stained with Rabbit anti-GABA (A2052; Sigma-Aldrich); ERK1/2 was stained with mouse anti-ERK1/2 (4696S; Cell Signaling Technology). The sRIMS solution, which is D-Sorbitol (Sigma-Aldrich) dissolved in PBS with 0.1% Tween-20 (Fisher Scientific) and 0.01% Sodium Azide, was used for optical clearing (Yang et al., 2014). Samples are immersed for 15 min (or until sunken to the bottom of the Eppendorf tube) through a gradient series (8.75% to 70%) of D-Sorbitol.

Image acquisition

Epifluorescence images of cultured cells were acquired under a Nikon Eclipse Ts2 inverted fluorescent microscope. Images of zebrafish were acquired using a Nikon A1 laser scanning confocal system with a CFI75 Apochromat LWD 25x water-immersion objective. For TRAS quantification, image stacks were acquired at a standard resolution of 0.49 x 0.49 x 2.0 μm^3 per voxel. For efferent tract tracing, a standard resolution stack and a high-resolution stack (0.38 x 0.38 x 0.5 μm^3 per voxel) were acquired for each fish.

Efferent tract tracing

Standard resolution image stacks were morphed to the Z-Brain *elavl3:H2B-RFP* template using CMTK (Randlett et al., 2015). High-resolution stacks were then morphed to its corresponding low-resolution stacks to register to Z-Brain coordinates. Morphed high-resolution stacks were imported into the neuTube software for tracing, in accordance with the neuTube online manual (https://www.neutracing.com/manual/) (Feng et al., 2015). The SWC files were saved and imported into Fiji plugin "Simple Neurite Tracer" then saved as an overlay.

TRAS quantitation with Z-Brain

Image stacks used for cell-type characterization were morphed to the Z-Brain *elavl3:H2B-RFP* template using CMTK, using the GCaMP6f channel as reference (Randlett et al., 2015). After morphing, the Fiji software's ROI manager (Analyze>Tools>ROI manager; extra-large size dot) was used on the VSVΔG channel to mark all VSVΔG+ cells. The marked positions (ROIs) were saved into a zip file and overlaid onto the GCaMP6f channel. The ROIs that were GCaMP6f-negative

were removed so that the remaining ROIs represented TRAS-labeled neurons (neuronal ROIs). Next, the neuronal ROIs were overlayed onto the GABA channel to create two subsets: the GABA+ ROIs (inhibitory neurons) and GABA- ROIs (excitatory neurons, created by subtracting the neuronal ROI with the GABA+ ROIs). Lastly, these two ROIs were overlaid onto a Z-brain reference-sized (X:Y:Z=1121x496x276 μm^3 at 0.8x0.8x2 μm^3 per voxel) blank stack, with inhibitory neuron ROIs pseudocolored magenta and excitatory neuron ROIs pseudocolored green.

To quantitate the anatomical distribution of retinorecipient cells, we followed the procedures for Z-Brain MAP-map analysis, but with several modifications (Randlett et al., 2015). Instead of using the MakeTheMAPmap.m MATLAB script, we used a custom Fiji macro script to create an image file. The image file which was quantified using a modified ZBrainAnalysisOfMAPmaps.m script that quantify sum pixel intensity values for neuronal ROIs within each region mask. The output Intensity values were converted to cell counts, based on an estimate of the pixel values generated from a single-cell ROI (~18,265). For heatmap display and cohort-wise comparison of individual regions, the intensity signals for each fish were normalized by the total signal from “Diencephalon” and “Mesencephalon.” The numbers were then imported into MATLAB to make a scaled color map using “imagesc” function.

Analysis of topographical distribution

To analyze the topographical distribution of wild-type and *dscaml1-/-* retinorecipient cells (Fig. 5), the ROI files from all fish within a cohort were combined into a single zip file and overlayed into a Z-Brain compatible blank stack, as described previously for single fish ROI image files. ROI

files from individual fish from the same genotype were combined into a single zip file. The x-y-z coordinates of each ROI dot were used in "scatter3" function in MATLAB to create 3-D scatter plots. The same coordinates were imported into GraphPad for analysis of distribution properties. The cumulative frequency statistics were done using the K-S test provided within the Prism software (GraphPad).

Excitatory/Inhibitory ratio

The total number of neurons in the *dscaml1-/-* cohort (267) was normalized to the total number of wild-type neurons (340), and the normalized increase of 27.34% in mutants was proportionally applied to individual anatomical regions and rounded up to a whole number. Excitatory-to-inhibitory neuron number ratios were calculated based on the estimated number of neurons within each anatomical region. In order to obtain valid ratio values, only regions with non-zero values were used for ratio analysis.

Results

Trans-complementation of VSVΔG by VSV-G coated lentivirus

For both VSV and RABV, the envelope glycoprotein (G) gene is essential for binding, internalization, membrane fusion, and release of the viral genome into the host cell (Albertini et al., 2012; Kim et al., 2017). A recombinant virus with genomic deletion of the G gene (ΔG) can infect and replicate inside the cell but is unable to spread, unless the host cell complements the

241 virus by providing G *in trans* (Wickersham et al., 2007; Beier et al., 2011b). Trans-
242 complementation can, therefore, be utilized to restrict viral spread to direct synaptic partners.
243 For instance, expressing the RABV-derived glycoprotein (RABV-G) in neurons at the injection site
244 (starter cells) allowed VSVΔG or RABVΔG to spread from the starter cells to their input neurons.
245 Once inside the input neurons, the virus can no longer spread (Wickersham et al., 2007; Beier et
246 al., 2013).

247 Given VSV's ability to spread anterogradely across synapses, we asked whether trans-
248 complementing VSVΔG virus with VSV glycoprotein (VSV-G) could enable restricted anterograde
249 spread (Mundell et al., 2015). Our efforts to express VSV-G *in vivo* through transgenesis was
250 unsuccessful, possibly due to the pathogenic effects of VSV-G when persistently expressed (Yee
251 et al., 1994). As an alternative, we tested whether VSV-G protein could be transduced to cells
252 directly. We took advantage of the fact that most commercially available lentiviruses are coated
253 with VSV-G and examined *in vitro* whether concomitant VSVΔG/lentivirus infection could provide
254 sufficient VSV-G to trans-complement VSVΔG. 293T cells were co-infected with VSV-G enveloped,
255 RFP-expressing VSVΔG at low density [multiplicity of infection (m.o.i.) = 0.005] and lentivirus at a
256 range of densities (m.o.i. = 0 to 1,000). At two days post-infection (dpi), we visualized the spread
257 of VSVΔG by fluorescent microscopy and determined the yield of newly synthesized VSVΔG in the
258 media. Indeed, lentivirus complemented VSVΔG in a dose-dependent manner, indicating that
259 VSV-G on the envelope of lentivirus could be taken up by VSVΔG to form functional virions (Fig.
260 1A-C).

Lentivirus-mediated trans-complementation was also effective *in vivo*, enabling transneuronal spread. By itself, VSVΔG injection (0.5 nl at 10^8 ffu/ml) into the eye resulted in retina infection and RFP labeling of the optic nerve, but no cellular labeling in the brain (Fig. 1D-E). This suggested that VSVΔG was not released from axon terminals to initiate a new cycle of infection in the brain. When low ($5x10^9$ ffu) or high titer lentivirus ($2x10^{10}$ ffu) was co-injected with VSVΔG (10^8 ffu/ml), we observed cellular labeling in the brain in both conditions, with more spread in injections with high titer lentivirus (Fig. 1F-G). This agrees with our *in vitro* results and indicates that high titer lentivirus can trans-complement VSVΔG, allowing viral spread from axon terminals.

The ability of lentivirus to trans-complement was not dependent on what the lentivirus genome encodes. Two types of VSV-G coated lentivirus were tested (lentivirus-SIN-CMV-eGFP and lentivirus-SIN-Ubi-iCre-mCherry). Both were able to mediate trans-complementation, and neither were able to drive transgene expression (eGFP and iCre-mCherry, respectively) on their own in fish at 6 dpi. Lastly, we asked whether VSVΔG could self-complement at higher titer since VSVΔG itself was also enveloped in VSV-G. Indeed, high titer VSVΔG ($2x10^9$ ffu/ml) could spread from the RGC to retinorecipient cells in the brain (Fig. 1H). Together, these results show that VSV-G from different viral particles could be recycled to form infectious VSV particles.

Restricted anterograde spread of VSVΔG in the zebrafish visual pathway

Since lentivirus was supplied at the injected site, only neurons at the injection site (starter cells) should be able to mediate spread. The spread from the starter cells should be limited to

direct postsynaptic targets, i.e., anterograde monosynaptic spread. To test this, we examined whether the spatial and temporal patterns of VSVΔG spread were consistent with monosynaptic spread from retinal ganglion cells (RGCs) to retinorecipient neurons in the brain.

VSVΔG and lentivirus were coinjected into anesthetized 3 dpf zebrafish larvae, followed by live confocal imaging at different time points (n=8 animals). Initial RFP expression from VSVΔG was present in the injected (left) eye as early as 5-hours post infection (hpi) (Fig. 1I). Cellular labeling in the contralateral (right) brain was observed at 1 dpi, and more cells were labeled at 3 dpi (Fig. 1J-K). At 6 dpi, there was no further spread to other brain regions, compared to 3 dpi (Fig. 1L). This pattern of labeling is distinct from non-G-deleted (replication competent) VSV, which rapidly progressed from axonal labeling to cell body labeling in downstream areas like the cerebellum and habenula at 3 dpi (Mundell et al., 2015). These results suggest that lentivirus trans-complementation primarily mediated anterograde monosynaptic spread. We call this new technique Tracer with Restricted Anterograde Spread (TRAS, pronounced like *trace*).

Efferent projections of retinorecipient cells were revealed by TRAS

Retinorecipient cells extend axons to different parts of the brain to mediate visually guided cognitive, sensory, motor, and homeostatic functions. Previous studies have utilized transgenic reporter lines to characterize efferent projections of subsets of retinorecipient cells, but there has not been a method that could unbiasedly label retinorecipient cells in different brain regions and reveal their efferent projections (Zhang et al., 2017; Helmbrecht et al., 2018; Kramer et al., 2019). With TRAS, we observed several prominent efferent tracts from retinorecipient neurons,

innervating the telencephalon (6 of 8 animals), habenula (2 of 8), midbrain tegmentum (7 of 8), contralateral optic tectum (7 of 8), cerebellum (6 of 8), and along the ventral hindbrain (6 of 8) (Fig. 2, image stack for panel 2A is shown in supplementary video 1). These projection patterns are reminiscent of the efferent projections of tectal/pretectal retinorecipient neurons, further supporting the idea that TRAS primarily labels retinorecipient cells (Sato et al., 2007; Mundell et al., 2015; Helmbrecht et al., 2018; Kramer et al., 2019). The projection into the telencephalon by retinorecipient neurons, to our best knowledge, has not been reported previously. These axon projections extend rostrally to enter the subpallium and then courses dorsally to the caudal pallium. Some axons crossed near the anterior commissure. These pallium-projecting neurons may serve similar roles as the mammalian lateral geniculate neurons to relay sensory information to higher visual areas (Mueller, 2012). These results show that TRAS could be used to identify not only postsynaptic cells but also downstream areas innervated by these cells.

3D mapping and cell-type characterization

To quantify connectivity patterns, we registered TRAS-labelled image stacks to the Z-Brain zebrafish brain atlas (Randlett et al., 2015). Transgenic fish expressing neuronal-localized nuclear GCaMP6f (*elavl3:H2B-GCaMP6f*) were injected at 2.5 dpf, into the temporal region of the left eye (representing the frontal visual field). Infected larvae were fixed at 3 dpi and stained with anti-GFP (to amplify the GCaMP6f signal) and anti-GABA. Stained samples were then cleared in sRIMS, a sorbitol-based mounting media that was crucial to resolving single cells and axon tracts in the ventral brain (Yang et al., 2014) (Fig. 3A-B, Supplementary Figure S2). By extracting the Z-Brain *elavl3:H2B-RFP* stack from ZBrainViewer as the reference, image stacks were morphed and

322 aligned with the Computational Morphometry Toolkit (CMTK) (Rohlfing and Maurer, 2003; Jefferis
323 et al., 2007; Randlett et al., 2015).

324 To distinguish between different cell types, both transgenic and immunohistochemical
325 markers were used. Nuclear GCaMP6f (expressed only in neurons) was used to distinguish
326 between neuronal (GCaMP6f+) and non-GCaMP (GCaMP6f-, non-neuronal cells and HuC-
327 neurons) cells. Anti-GABA staining was used to distinguish between non-GABAergic and
328 GABAergic (inhibitory) neurons (Cui et al., 2005) (Fig. 3C). Since glycinergic neurons are not
329 present in the retinorecipient areas, non-GABAergic retinorecipient neurons are predominantly
330 excitatory. After CMTK, all TRAS labeled cells were converted into Z-Brain coordinates and
331 categorized into three types: excitatory neurons (GCaMP6f+, GABA-) inhibitory neurons
332 (GCaMP6f+, GABA+), and non-GCaMP cells. In total, 24 wild-type and 26 *dscaml1-/-* fish (see next
333 section) were analyzed (Fig. 4A-B, supplementary video 2, supplemental Figure S3). The overall
334 ratio of excitatory versus inhibitory cells was similar between wild-type and *dscaml1-/-* cohorts
335 (p=0.515, Chi-square= 0.424). The annotated stack could be viewed with the Z-Brain off-line
336 viewer and overlaid with anatomical annotations and reference stacks therein (Randlett et al.,
337 2015).

338 We also verified that Z-Brain registered stacks could be used as templates for tracing the
339 efferent projections of retinorecipient cells (Fig. 4C). We acquired both high-resolution and low-
340 resolution image stacks for the same fish and used the high-resolution image stacks for tracing
341 and low-resolution image stacks as the template to register to Z-Brain. We observed ipsilateral
342 and commissural axon tracts, with morphologies that are similar to the tectal efferent tracts

343 described in previous studies (Sato et al., 2007; Helmbrecht et al., 2018).

344 **Comparative analysis of retinofugal connectivity**

345 In addition to normal patterns of retinofugal connectivity, TRAS and Z-Brain can be used
346 to investigate retinofugal connectivity patterns in mutants with visual deficits. We focused on
347 *Down Syndrome Cell Adhesion Molecule Like-1* (*DSCAML1)*, a gene mutated in patients with
348 autism spectrum disorder, cortical abnormalities, and developmental disorders (Iossifov et al.,
349 2014; Karaca et al., 2015; Deciphering Developmental Disorders Study, 2017). In zebrafish,
350 *dscaml1* is broadly expressed in visual areas and required for visual and visuomotor behaviors,
351 suggesting an underlying visual circuit deficit (Ma et al., 2019). Therefore, we compared the
352 retinofugal connectivity patterns between 5.5 dpf wild-type fish and their *dscaml1* mutant
353 (*dscaml1-/-*) siblings.

354 We first asked whether loss of *dscaml1* affected the topographical distribution of
355 retinorecipient neurons (340 and 267 in wild type and *dscaml1-/-*, respectively) (Fig. 5). As the
356 initial site of viral infection was in the temporal retina, these retinorecipient neurons likely
357 respond to frontal visual stimulus. The overall distribution was similar between cohorts along the
358 three cardinal axes, but the proportion of retinorecipient cells was significantly shifted in the
359 rostral-caudal and lateral-medial axes. Along the rostral-caudal axis, both excitatory and
360 inhibitory retinorecipient neurons from the *dscaml1*-/- cohort were more rostrally distributed,
361 compared to wild type ($p<0.001$ and $p<0.05$ for excitatory and inhibitory neurons, respectively.
362 K-S test). Along the dorsal-ventral axis, the effect of *dscaml1* deficiency was milder. *dscaml1-/-*

363 retinorecipient cells were more dorsally distributed, compared to wild type, but only for
364 excitatory neurons ($p<0.05$, K-S test). There were no differences in lateral-medial distribution.
365 These results suggest that loss of *dscaml1* may affect the topographic mapping of visual inputs,
366 particularly along the rostral-caudal axes.

367 Next, we focused on the distribution of retinorecipient cells within specific annotated
368 brain regions. We adapted the Z-Brain quantification tools to measure the sum pixel intensity
369 derived from TRAS-labeled cells for each region (see methods). Among regions defined by
370 anatomy (i.e., not defined by transgene expression), 16 were found to contain, on average, at
371 least 1 retinorecipient cell per animal in the wild-type cohort (Fig. 6A, Supplementary Figure S4).
372 Two major brain divisions, the mesencephalon and rhombencephalon, encompassed all of the
373 retinorecipient cells. Within these divisions, the retinorecipient cells are located within
374 subregions corresponding to known to receive retinofugal input, including the preoptic area,
375 hypothalamus, thalamus, eminentia thalami, pretectum, and optic tectum (tectum neuropil,
376 tectum stratum periventriculare, and medial tectal band) (Burrill and Easter Jr, 1994; Zhang et al.,
377 2017; Helmbrecht et al., 2018; Kramer et al., 2019). We saw no cellular labeling in the olfactory
378 bulb (which innervates the retina), indicating that lentivirus complementation did not facilitate
379 retrograde spread (Li and Dowling, 2000). We also identified several retinorecipient areas that, to
380 the best of our knowledge, had not previously been identified (torus semicircularis, tegmentum,
381 posterior tuberculum).

382 In general, the same areas were innervated in both wild-type and *dscaml1-/-* cohorts,
383 except for two smaller areas that were not innervated in the *dscaml1-/-* cohort (eminentia

384 thalami and intermediate hypothalamus) (Fig. 6A-B). This result indicates that major
385 retinorecipient areas are innervated by the optic nerve in the *dscaml1-/-* animals. Interestingly,
386 the ratio of excitatory versus inhibitory retinorecipient cells (E/I ratio) was more variable in the
387 *dscaml1-/-* cohort, compared to wild type. This was true both for major brain divisions
388 (diencephalon vs. mesencephalon) and subregions (Fig. 6C-D). A possible explanation for this
389 might be that loss of *dscaml1* affects the targeting of specific cell types within each retinorecipient
390 region.

391 **TRAS mapping of habenular-recipient neurons**

392 Finally, to test whether TRAS can be applied more generally to other CNS neuronal
393 populations besides RGCs, we examined efferent targeting from the left habenula (Bianco and
394 Wilson, 2009; Amo et al., 2010; Lee et al., 2010; Dreosti et al., 2014; Duboue et al., 2017; Zhang
395 et al., 2017). The bilaterally asymmetrical habenula receives many different sensory cues and is
396 involved in processing social cues, fear learning, and avoidance. The left habenula is known
397 projects to the interpeduncular nucleus (IPN) and superior raphe, providing a suitable pathway
398 to test TRAS mapping (Bianco and Wilson, 2009; Amo et al., 2010). TRAS labeling and image
399 registration were performed as described above, except that virus were injected in the left
400 habenula of wild-type fish. Registered image stacks from five animals with selective left habenula
401 labeling were combined (Fig. 7A-B). We observed consistent labeling of the habenular axon tract
402 and the characteristic annular axon terminals in the IPN. Cell bodies near IPN axon terminals were
403 manually marked (Fig. 7C-D). Consistent with previous findings, habenular target cells we labeled
404 within the IPN and raphe nucleus (Amo et al., 2010). A group of labeled cells is located

405 immediately dorsal to the annotated superior raphe nucleus in Z-Brain, which are likely glial cells.
406 These results demonstrate the general applicability of TRAS for mapping targets of efferent axons.
407

408 Discussion

409 In this study, we developed TRAS, a new method for monosynaptic anterograde labeling
410 in larval zebrafish. This method was applied to the retinofugal pathway and also validated in the
411 habenula efferent pathway. We showed that TRAS could be combined with the Z-Brain image
412 registration and quantitation pipeline to identify changes in retinofugal connectivity patterns
413 caused by the loss of *dscaml1*. These results demonstrate the broad utility of TRAS for neural
414 circuit studies in zebrafish.

415 Trans-complementation of VSVΔG by lentivirus

416 The structure and function of VSV-G have been extensively studied in the context of viral
417 entry, membrane fusion, toxicity, and subcellular transport (Dotti and Simons, 1990; Thomas et
418 al., 1993; Ang et al., 2004; Hoffmann et al., 2010; Albertini et al., 2012; Fossati et al., 2014; Kim
419 et al., 2017). VSV-G also determines the infectivity of VSV-G coated viruses (VSV, RABV, lentivirus,
420 retrovirus), which is crucial for their research and clinical applications (Wickersham et al., 2013;
421 Amirache et al., 2014; Mundell et al., 2015; Kobayashi et al., 2016). Our findings revealed a new
422 aspect of VSV-G function, where VSV-G protein from a different viral species can be recycled to
423 generate infectious VSV.

The spread of VSVΔG from the retina to CNS neurons indicates that VSV-G on the lentivirus surface remained functional after lentivirus infection, and a portion of it was transported anterogradely from the cell body to the axon terminal. At the axon terminal, lentivirus-derived VSV-G was able to re-encapsulate the VSV nucleocapsid and mediate subsequent infection. The strategy of using lentivirus as a tool for glycoprotein complementation could potentially be applied more broadly. For example, current strategies for RABV monosynaptic tracing utilizes AAV to express RABV glycoprotein, which usually takes several weeks for sufficient glycoprotein expression (Miyamichi et al., 2011). It will be interesting to test whether rabies glycoprotein-coated lentivirus could be a more expedient method to provide glycoprotein for retrograde tracing.

Applying TRAS for zebrafish neural connectivity analysis

Advances in viral engineering have led to new neural circuit tracing strategies utilizing replication-incompetent viruses (e.g., RABV, AAV, HSV) that are safer to use, less toxic to host cells, and have restricted (mostly monosynaptic) spread (Wickersham et al., 2007; Zingg et al., 2017; Chatterjee et al., 2018; Beier, 2019). Unfortunately, many of the transsynaptic viruses used in mammalian systems either do not infect zebrafish (e.g., AAV) or have low efficiency for transsynaptic spread (e.g., RABV) (Zhu et al., 2009; Dohaku et al., 2019). VSV, in contrast, can infect larval zebrafish and spreads robustly both anterogradely and retrogradely. However, replication-competent VSV has high cytotoxicity and can spread across multiple synapses, making it difficult to distinguish between direct versus indirect connections (Mundell et al., 2015).

444 To address these limitations and provide a tool for neural circuit mapping for larval
445 zebrafish, we developed TRAS. TRAS utilizes recombinant VSV with genomic deletion of the
446 glycoprotein gene (VSVΔG). VSVΔG can infect cells at the injection site but cannot spread.
447 Although wild-type VSV does not cause serious illness to humans, the use of VSVΔG further
448 reduces the risk of exposure (Spickler, 2016). The lack of VSV-G expression from the viral genome
449 also helps reduces toxicity to the host cell, as long-term VSV-G expression is known to be cytotoxic
450 (Yee et al., 1994). To complement VSVΔG, we directly provided VSV-G protein, utilizing lentivirus
451 as the transducing reagent. Compared to transgenic or virus-induced expression, this approach is
452 rapid and transient, therefore minimizing the cellular exposure to VSV-G. Both VSVΔG and VSV-G
453 coated lentivirus are available from a commercial source, making TRAS an easy method to adopt
454 in a typical neuroscience laboratory.

455 To extend the utility of TRAS, we developed procedures to register brain images to the Z-
456 Brain anatomical template (Randlett et al., 2015). The combination of neural circuit tracing within
457 a standard 3D-brain atlas is the current state of the art approach for understanding neural
458 network connections, both in zebrafish and mammalian models (Watabe-Uchida et al., 2012; Oh
459 et al., 2014; Helmbrecht et al., 2018; Kramer et al., 2019; Kunst et al., 2019). This approach
460 provides a more objective way to map cells and pathways onto specific brain regions across
461 different experimental animals and promotes cross-referencing between research findings.

462 We demonstrated that TRAS and Z-Brain could be used for neural circuit mapping in
463 efferent pathways originating from the retina and the left habenula. These are two of the better-

studied pathways in larval zebrafish, which allowed us to assess the specificity of TRAS for anterograde labeling of direct postsynaptic targets. Overall, TRAS identified all of the target regions described in previous studies, which gives confidence to the future application of TRAS to map unknown neural connections in zebrafish. Furthermore, given that VSV is also an anterograde tracer in mice and chicken, it will be interesting to test whether TRAS can be applied to these experimental systems for neural circuit mapping (Mundell et al., 2015).

Limitations and the future development of TRAS

While TRAS offers many advantages as a neural circuit mapping tool, it is important to note some of the limitations of the technique. These are also areas with potential for further technological development. First, since VSV-G binds to a receptor that is widely expressed (LDL receptor) (Finkelshtein et al., 2013), VSV-G coated viruses (e.g., VSVΔG and lentivirus) can infect most cell types. Therefore, the specificity of TRAS depends on precise injection into the brain region of interest. For brain regions smaller than the habenula, a compound microscope with DIC optics would be necessary. To restrict infection to a particular cell type, it may be possible to make use of ASLV-A pseudotyped VSVΔG that can selectively target neurons expressing an exogenous receptor, TVA (Beier et al., 2011b; Dohaku et al., 2019). However, potential interactions between virions with different envelope glycoproteins may interfere with the specificity of VSVΔG infection (Beier et al., 2011a)

Second, while VSVΔG by itself cannot spread after initial infection, it can still replicate and change the metabolism of the host cell. For instance, the VSV M protein is capable of altering host

cell transcription and translation. Chronic VSVΔG infection would likely affect the survival of infected neurons and impair its neurophysiological functions. Several approaches for reducing the toxicity of RABV have been reported recently to reduce the function or expression of viral proteins, such as destabilizing the RABV nucleoprotein or deleting the RABV L gene (Ciabatti et al., 2017; Chatterjee et al., 2018). Similar manipulations may also reduce the toxicity of VSV.

Third, we observed TRAS labeling of cells that do not express the *HuC:H2B-GCaMP6f* transgene (non-GCaMP cells), which may be glial cells. While not frequently discussed, viral transmission from neuron to glia does occur for most viral transsynaptic tracers, including PRBV, HSV, RABV, and VSV (Beier, 2019). In a replication-competent virus, the infection of glia and subsequent spread to neurons would make it challenging to infer connectivity. This issue is circumvented in TRAS, as VSVΔG cannot spread after glial infection (due to the lack of VSV-G). Nevertheless, this highlights the importance of distinguishing bona fide neurons versus other cell types in any type of transsynaptic labeling study.

Lastly, quantitation by Z-Brain depends on morphing and registration of image stacks to a reference template, followed by manual identification of labeled neurons. This approach is suitable to test the effects of single genes or pathological states, but likely too laborious as a screening tool to identify candidate genes or screen drugs. Selective fluorescent labeling of neuronal cell bodies (without labeling neurites) and automation of cell detection would be a crucial next step to improve the utility of TRAS.

Connectivity patterns associated with *dscaml1* deficiency

The ability to quantitate efferent connections prompted us to investigate whether TRAS can be used to identify connectivity deficits caused by *dscaml1* deficiency. As mentioned previously, human DSCAML1 mutations are believed to be causative for neurodevelopmental disorders. Additionally, our recent work has found that loss of *dscaml1* significantly impaired visuomotor function associated with light perception and eye movements, suggesting a possible underlying deficit along the visual pathway (Ma et al., 2019).

Using TRAS and Z-Brain quantification, we found that *dscaml1* deficiency might have a role in refining the retinofugal topography and cell-type specificity. On a broader scale, we saw similar patterns of topographic and region-specific projections between wild-type and *dscaml1-/-* cohorts (Fig. 6, 7). This indicated that RGC axonal targeting was mostly intact in the *dscaml1* mutants. Interestingly, there was a significant rostral shift in the position in both excitatory and inhibitory retinorecipient cells. Given that RGC axon terminals and retinorecipient cells are both topographically organized, this shift in positioning may result in diminished spatial perception (Stuermer, 1988; Muto et al., 2013; Robles et al., 2014). We also observed a trend for altered ratio of excitatory versus inhibitory retinorecipient cells in the *dscaml1* mutants. For example, the preoptic area and tegementum have higher a ratio of inhibitory neurons in the *dscaml1* mutants, compared to wild type. This putative change in retinofugal target selection could lead to network changes and altered visual response. Further physiological studies will be needed to formally test whether *dscaml1* affects spatial perception and the excitatory/inhibitory balance in the visual pathway.

524 **Conclusions**

525 Here we present the development of a new technique (TRAS) that is suitable for mapping
526 neural connectivity in zebrafish. TRAS makes use of a novel lentivirus trans-complementation
527 approach to enable restricted anterograde transneuronal spread by recombinant VSV. We have
528 validated this method in two efferent pathways and identified potential connectivity pattern
529 changes caused by a genetic deficiency in *dscaml1*, a neuronal cell adhesion molecule associated
530 with human neurodevelopmental disorders. The ability of TRAS to map structural connectivity
531 would enable the discovery of new neural connections and complement existing brain mapping
532 efforts.

533 ## Author Contributions

534 M.M., S.K., and Y.A.P. conceived the study, performed the experiments, and analyzed the data.
535 S.K. prepared and characterized recombinant viruses. M.M. and Y.A.P. wrote the manuscript, with
536 contributions from S.K.

537 ## Figure Legends

538 **Figure. 1. Lentivirus enabled in vitro and in vivo trans-complementation of VSVΔG and**
539 **transneuronal spread. A-C**, lentivirus trans-complementation in vitro. VSVΔG was able to infect
540 293T cells but was unable to spread to neighboring cells, as evident by sparse single-cell infections.
541 (A). In conjunction with lentivirus, VSVΔG was able to both infect and spread, as evident by the
542 presence of large infected plaques (B). The extent of VSVΔG amplification (as measured by viral

titer) is positively correlated with lentivirus titer, expressed in m.o.i. (C). **D,** Illustration of viral injection and labeling of the optic nerve. Virus was microinjected into the left eye, which infected the RGC and resulted in fluorescent labeling of the RGC axons (i.e., optic nerve, magenta). The layout of the larval CNS is labeled in green, with the olfactory bulb (OB), pallium (P), habenula (H), optic tectum (OT), and cerebellum (Cb) labeled. **E-H,** In vivo trans-complementation and spread of VSVΔG by lentivirus. In the absence of lentivirus, VSVΔG infected RGCs and fluorescently labeled the optic nerve, but no spread in the CNS was observed (E). When lentivirus and VSVΔG were coinjected, cellular labeling was observed in the CNS (yellow arrowheads), indicating transneuronal spread. Similar patterns of spread was also seen at very high VSVΔG titer ($2x10^9$ versus 10^8 ffu/ml for panels E-G), suggesting that VSVΔG was able to self-complement (H). **I-L,** Time course of VSVΔG infection and spread with lentivirus trans-complementation, with RFP expression from VSVΔG (magenta) and GFP expression from the *vglut2a:GFP* transgene (green). Box regions are shown at higher magnifications below (I'-L'). Scale bars are 100 μm. Images in the same row are shown at the same scale.

Figure 2. Efferent projections of retinorecipient cells. A-A', Confocal maximal intensity projection (dorsal view) of TRAS-labeled larva, with RFP expression from VSVΔG in magenta (A) or white (A'). Axon projections can be seen in the pallium (P), optic tectum (OT), cerebellum (Cb), and hindbrain (Hb). **B-E,** Maximal intensity projection confocal substacks that contained the pallium (B), habenula (C), hypothalamus (D), and cerebellum (E). RFP expression from VSVΔG (magenta) and GFP expression from the *vglut2a:GFP* transgene (green) are shown in B-E, while boxed region is

563 shown at higher magnification in B'-E', with only the RFP channel (white). Scale bars are 100 μm
564 in A and B, and 50 μm in B'. Images in the same row are shown at the same scale.

565 **Figure 3. Cell-type characterization of TRAS labeling. A,** The workflow for TRAS labeling, tissue
566 processing, image acquisition, and data analysis. **B,** Orthogonal views of an imaged fish after
567 tissue clearing with sRIMS. Orthogonal views (XY, XZ, and YZ) of confocal image stacks are shown.
568 **C-C',** Cytochemical characterization of TRAS-labeled cells. A single confocal imaging plane is
569 shown, with merged, GCaMPf, GABA, and VSVΔG channels as indicated. Boxed area in C is shown
570 in higher magnification in C'. The purple arrowhead marks a GCaMP6f+/GABA+/VSVΔG+
571 inhibitory neuron. The yellow arrowhead marks a GCaMP6f+/GABA-/VSVΔG+ excitatory neuron.
572 Scale bars are 100 μm.

573 **Figure 4. Annotation of TRAS-labeled neurons and efferent axons in the Z-Brain standard brain**
574 **reference. A,** Overview of all annotated TRAS-labeled retinorecipient cells within the wild-type
575 and *dscaml1-/-* cohorts. **B,** Spatial layout of TRAS-labeled neurons (dorsal view, rostral to the left)
576 overlayed onto the Z-brain reference brain scale, for wild-type (top row) and *dscaml1-/-* (bottom
577 row) cohorts. Green dots mark excitatory neurons, magenta dots mark inhibitory neurons. **C-E,**
578 Efferent tract tracing from wild-type larvae (n=10). Maximum Z-projection is shown for confocal
579 image (C), traced ipsilateral tracts (D), and commissural tracts (E). Axons with similar trajectories
580 are displayed in the same color. Scale bars are 100um.

581 **Figure 5. Topographical organization of retinorecipient neurons in wild-type and *dscaml1-/-***
582 **cohorts.** Graphs show the topographical distribution of excitatory (A, B) and inhibitory neurons

(C, D) in wild-type (black, n=24) and *dscaml1-/-* (red, n=26) cohorts. Axes are relative distances (pixels) within the Z-Brain reference brain stack. **A, C,** Three-dimensional distribution of excitatory (A) and inhibitory (C) neurons. **B, D,** Frequency distributions of excitatory (B) and inhibitory (D) neurons in the rostral-caudal, dorsal-ventral, and lateral-medial axes. Dashed lines indicate the boundary between the diencephalon and the mesencephalon. K-S test, *: P<0.05 ; ***: P<0.001.

Figure 6 Retinorecipient cell distribution and excitatory-inhibitory balance in major anatomical regions. A-B, Axes show estimated cell numbers (converted from intensity signals) in each region in wild-type (A, n=24) and *dscaml1-/-* (B, n=26) cohorts. **C-D,** Excitatory/inhibitory ratio for all labeled non-zero regions in both wild-type (n=24) and *dscaml1-/-* (n=26), listed in **A** and **B**. **C,** Excitatory/inhibitory ratio comparison of diencephalon and mesencephalon. **D,** Excitatory/inhibitory ratio comparison of subregions within diencephalon and mesencephalon.

Figure 7. TRAS labeling of habenular target cells. Dorsal views (A-B, C-D) and lateral views (A'-B', C'-D') are shown. **A-B,** Maximal projection of registered image stacks from animals with initial infection in the left habenula (arrowhead). Habenular efferent tract projects into the IPN (arrow). RFP expression from VSVΔG infection is shown in magenta (A-A') or white (B-B'). For anatomical reference, images are overlaid on top of the Z-Brain ERK1/2 reference stack (green, A-A'), or region outlines for the habenula (yellow), IPN (cyan), and raphe nucleus (red) (B-B'). **C-D,** Manually marked habenular target cells (magenta in C-C', white in D-D') are overlaid on top of anatomical references, as described for panels A-B. Scale bars are 100 μm. All images are shown at the same scale.

603 **Supplementary Figure S1. Examples of secondary TRAS labeling.** Red arrowheads indicate
604 secondary spread due to a higher titer of virus. Yellow dash line marks the border of
605 mesencephalon and cerebellum. Scale bar: 50 μm.

606 **Supplementary Figure S2. Tissue clearing with sRIMS solution.** Whole-mount ERK1/2
607 immunolabeling without (A) or with sRIMS clearing (B). Orthogonal views (XY, XZ, and YZ) of
608 confocal image stacks are shown, centered just bellowed the cerebellum (intersect of yellow lines).
609 Ventral structures are not visible without sRIMS clearing. Scale bars are 100 μm.

610 **Supplementary Figure S3. TRAS labeling of non-neuronal cells.** A single confocal imaging plane
611 is shown, with merged, GCaMPf, GABA, and VSVΔG channels as indicated. Boxed area in A is
612 shown in higher magnification in A'. The purple arrowheads mark two
613 GCaMP6f+/GABA+/VSVΔG+ inhibitory neurons. The orange arrowhead marks a GCaMP6f-/GABA-
614 /VSVΔG+ cell. Scale bars are 100 μm.

615 **Supplementary Figure S4. Signals detected via Z-brain in wild-type and *dscaml1-/-* fish. A-B,**
616 Heat map of normalized signals in major anatomical regions from Z-brain showing normalized
617 signals detected within each sample used for analysis, wild-type (n=24) and *dscaml1-/-* (n=26),
618 and their corresponding neuron types **A** is excitatory while **B** is inhibitory. All signals were
619 descended aligning to Diencephalon.

620

Videos

Supplementary Video 1. Image stack of TRAS-labeled zebrafish larva, three days after the initial infection. VSVΔG labeling is shown in magenta and *vglut2a:GFP* labeling in green.

Supplementary Video 2. Excitatory (green) and inhibitory (magenta) retinorecipient cells in wild type (left) and *dscaml1-/-* (right) cohorts. ERK1/2 immunolabeling (white) from Randlett et al. 2015 is overlaid to serve as an anatomical reference.

Data Availability

The image stacks and other data supporting the findings of this study are available from the corresponding author upon reasonable request.

Code Availability

Custom Fiji and MATLAB scripts used of this study are available from the corresponding author upon reasonable request.

References

Abdelfattah AS et al. (2019) Bright and photostable chemigenetic indicators for extended in vivo voltage imaging. Science 365:699-704.

Ahrens MB, Orger MB, Robson DN, Li JM, Keller PJ (2013) Whole-brain functional imaging at cellular resolution using light-sheet microscopy. Nat Methods 10:413-420.

Albertini AA, Baquero E, Ferlin A, Gaudin Y (2012) Molecular and cellular aspects of rhabdovirus entry. Viruses 4:117-139.

Amirache F, Lévy C, Costa C, Mangeot P-E, Torbett BE, Wang CX, Nègre D, Cosset F-L, Verhoeyen E (2014) Mystery

643 solved: VSV-G-LVs do not allow efficient gene transfer into unstimulated T cells, B cells, and HSCs because
644 they lack the LDL receptor. Blood 123:1422.
645 Amo R, Aizawa H, Takahoko M, Kobayashi M, Takahashi R, Aoki T, Okamoto H (2010) Identification of the zebrafish
646 ventral habenula as a homolog of the mammalian lateral habenula. J Neurosci 30:1566-1574.
647 Ang AL, Taguchi T, Francis S, Folsch H, Murrells LJ, Pypaert M, Warren G, Mellman I (2004) Recycling endosomes can
648 serve as intermediates during transport from the Golgi to the plasma membrane of MDCK cells. J Cell Biol
649 167:531-543.
650 Bae YK, Kani S, Shimizu T, Tanabe K, Nojima H, Kimura Y, Higashijima S, Hibi M (2009) Anatomy of zebrafish cerebellum
651 and screen for mutations affecting its development. Dev Biol 330:406-426.
652 Beier KT (2019) Hitchhiking on the neuronal highway: Mechanisms of transsynaptic specificity. Journal of chemical
653 neuroanatomy 99:9-17.
654 Beier KT, Samson MES, Matsuda T, Cepko CL (2011a) Conditional expression of the TVA receptor allows clonal analysis
655 of descendents from Cre-expressing progenitor cells. Developmental Biology 353:309-320.
656 Beier KT, Mundell NA, Pan YA, Cepko CL (2016) Anterograde or Retrograde Transsynaptic Circuit Tracing in Vertebrates
657 with Vesicular Stomatitis Virus Vectors. Curr Protoc Neurosci 74:1 26 21-27.
658 Beier KT, Saunders AB, Oldenburg IA, Sabatini BL, Cepko CL (2013) Vesicular stomatitis virus with the rabies virus
659 glycoprotein directs retrograde transsynaptic transport among neurons in vivo. Frontiers in neural circuits
660 7:11.
661 Beier KT, Saunders A, Oldenburg IA, Miyamichi K, Akhtar N, Luo L, Whelan SP, Sabatini B, Cepko CL (2011b)
662 Anterograde or retrograde transsynaptic labeling of CNS neurons with vesicular stomatitis virus vectors.
663 Proceedings of the National Academy of Sciences of the United States of America 108:15414-15419.
664 Belmonte MK, Allen G, Beckel-Mitchener A, Boulanger LM, Carper RA, Webb SJ (2004) Autism and abnormal
665 development of brain connectivity. J Neurosci 24:9228-9231.
666 Bianco IH, Wilson SW (2009) The habenular nuclei: a conserved asymmetric relay station in the vertebrate brain.
667 Philosophical transactions of the Royal Society of London Series B, Biological sciences 364:1005-1020.
668 Burrill JD, Easter Jr SS (1994) Development of the retinofugal projections in the embryonic and larval zebrafish
669 (Brachydanio rerio). Journal of Comparative Neurology 346:583-600.
670 Chatterjee S et al. (2018) Nontoxic, double-deletion-mutant rabies viral vectors for retrograde targeting of projection
671 neurons. Nat Neurosci.
672 Chen X, Mu Y, Hu Y, Kuan AT, Nikitchenko M, Randlett O, Chen AB, Gavornik JP, Sompolinsky H, Engert F, Ahrens MB
673 (2018) Brain-wide Organization of Neuronal Activity and Convergent Sensorimotor Transformations in Larval
674 Zebrafish. Neuron 100:876-890 e875.
675 Ciabatti E, Gonzalez-Rueda A, Mariotti L, Morgese F, Tripodi M (2017) Life-Long Genetic and Functional Access to
676 Neural Circuits Using Self-Inactivating Rabies Virus. Cell 170:382-392.e314.
677 Cui WW, Low SE, Hirata H, Saint-Amant L, Geisler R, Hume RI, Kuwada JY (2005) The Zebrafish shocked
678 Gene Encodes a Glycine Transporter and Is Essential for the Function of Early Neural Circuits in the CNS. The
679 Journal of Neuroscience 25:6610-6620.
680 Deciphering Developmental Disorders Study (2017) Prevalence and architecture of de novo mutations in
681 developmental disorders. Nature 542:433-438.
682 Dohaku R, Yamaguchi M, Yamamoto N, Shimizu T, Osakada F, Hibi M (2019) Tracing of Afferent Connections in the
683 Zebrafish Cerebellum Using Recombinant Rabies Virus. Frontiers in neural circuits 13:30.
684 Dotti CG, Simons K (1990) Polarized sorting of viral glycoproteins to the axon and dendrites of hippocampal neurons
685 in culture. Cell 62:63-72.
686 Dreosti E, Vendrell Llopis N, Carl M, Yaksi E, Wilson SW (2014) Left-right asymmetry is required for the habenulae to
687 respond to both visual and olfactory stimuli. Curr Biol 24:440-445.
688 Duboue ER, Hong E, Eldred KC, Halpern ME (2017) Left Habenular Activity Attenuates Fear Responses in Larval
689 Zebrafish. Curr Biol 27:2154-2162 e2153.
690 Feng L, Zhao T, Kim J (2015) neuTube 1.0: A New Design for Efficient Neuron Reconstruction Software Based on the
691 SWC Format. eNeuro 2.
692 Finkelshtein D, Werman A, Novick D, Barak S, Rubinstein M (2013) LDL receptor and its family members serve as the

693 cellular receptors for vesicular stomatitis virus. Proceedings of the National Academy of Sciences of the
694 United States of America 110:7306-7311.
695 Fornito A, Zalesky A, Breakspear M (2015) The connectomics of brain disorders. Nature Reviews Neuroscience 16:159.
696 Fossati M, Colombo SF, Borgese N (2014) A positive signal prevents secretory membrane cargo from recycling
697 between the Golgi and the ER. Embo j 33:2080-2097.
698 Fuerst PG, Bruce F, Tian M, Wei W, Elstrott J, Feller MB, Erskine L, Singer JH, Burgess RW (2009) DSCAM and DSCAML1
699 function in self-avoidance in multiple cell types in the developing mouse retina. Neuron 64:484-497.
700 Galicia CA, Sukeena JM, Stenkamp DL, Fuerst PG (2018) Expression patterns of dscam and sdk gene paralogs in
701 developing zebrafish retina. Molecular vision 24:443-458.
702 Glasser MF, Coalson TS, Robinson EC, Hacker CD, Harwell J, Yacoub E, Ugurbil K, Andersson J, Beckmann CF, Jenkinson
703 M, Smith SM, Van Essen DC (2016) A multi-modal parcellation of human cerebral cortex. Nature 536:171.
704 Helmbrecht TO, Dal Maschio M, Donovan JC, Koutsouli S, Baier H (2018) Topography of a Visuomotor Transformation.
705 Neuron.
706 Hildebrand DGC et al. (2017) Whole-brain serial-section electron microscopy in larval zebrafish. Nature 545:345-349.
707 Hoffmann M, Wu YJ, Gerber M, Berger-Rentsch M, Heimrich B, Schwemmle M, Zimmer G (2010) Fusion-active
708 glycoprotein G mediates the cytotoxicity of vesicular stomatitis virus M mutants lacking host shut-off activity.
709 The Journal of general virology 91:2782-2793.
710 Iossifov I et al. (2014) The contribution of de novo coding mutations to autism spectrum disorder. Nature 515:216-
711 221.
712 Jefferis GS, Potter CJ, Chan AM, Marin EC, Rohlfing T, Maurer CR, Jr., Luo L (2007) Comprehensive maps of Drosophila
713 higher olfactory centers: spatially segregated fruit and pheromone representation. Cell 128:1187-1203.
714 Karaca E et al. (2015) Genes that Affect Brain Structure and Function Identified by Rare Variant Analyses of Mendelian
715 Neurologic Disease. Neuron 88:499-513.
716 Kasthuri N et al. (2015) Saturated Reconstruction of a Volume of Neocortex. Cell 162:648-661.
717 Kawashima T, Zwart MF, Yang CT, Mensh BD, Ahrens MB (2016) The Serotonergic System Tracks the Outcomes of
718 Actions to Mediate Short-Term Motor Learning. Cell 167:933-946 e920.
719 Kim IS, Jenni S, Stanifer ML, Roth E, Whelan SP, van Oijen AM, Harrison SC (2017) Mechanism of membrane fusion
720 induced by vesicular stomatitis virus G protein. Proceedings of the National Academy of Sciences of the
721 United States of America 114:E28-E36.
722 Kimmel CB, Ballard WW, Kimmel SR, Ullmann B, Schilling TF (1995) Stages of embryonic development of the zebrafish.
723 Dev Dyn 203:253-310.
724 Kobayashi K, Kato S, Inoue K, Takada M, Kobayashi K (2016) Altering Entry Site Preference of Lentiviral Vectors into
725 Neuronal Cells by Pseudotyping with Envelope Glycoproteins. Methods in molecular biology 1382:175-186.
726 Kramer A, Wu Y, Baier H, Kubo F (2019) Neuronal Architecture of a Visual Center that Processes Optic Flow. Neuron.
727 Kunst M, Laurell E, Mokayes N, Kramer A, Kubo F, Fernandes AM, Förster D, Dal Maschio M, Baier H (2019) A Cellular-
728 Resolution Atlas of the Larval Zebrafish Brain. Neuron.
729 Lee A, Mathuru AS, Teh C, Kibat C, Korzh V, Penney TB, Jesuthasan S (2010) The habenula prevents helpless behavior
730 in larval zebrafish. Curr Biol 20:2211-2216.
731 Li L, Dowling JE (2000) Disruption of the olfactoretinal centrifugal pathway may relate to the visual system defect in
732 night blindness b mutant zebrafish. J Neurosci 20:1883-1892.
733 Lynall M-E, Bassett DS, Kerwin R, McKenna PJ, Kitzbichler M, Muller U, Bullmore E (2010) Functional Connectivity and
734 Brain Networks in Schizophrenia. The Journal of Neuroscience 30:9477-9487.
735 Ma M, Ramirez AD, Wang T, Roberts RL, Harmon KE, Schoppik D, Sharma A, Kuang C, Goei SL, Gagnon JA, Zimmerman
736 S, Tsai SQ, Reyon D, Joung JK, Aksay ERF, Schier AF, Pan YA (2019) Zebrafish Dscaml1 is Essential for Retinal
737 Patterning and Function of Oculomotor Subcircuits. bioRxiv:658161.
738 Maack G, Segner H (2003) Morphological development of the gonads in zebrafish. Journal of Fish Biology 62:895-
739 906.
740 Miyamichi K, Amat F, Moussavi F, Wang C, Wickersham I, Wall NR, Taniguchi H, Tasic B, Huang ZJ, He Z, Callaway EM,
741 Horowitz MA, Luo L (2011) Cortical representations of olfactory input by trans-synaptic tracing. Nature
742 472:191-196.

Mueller T (2012) What is the Thalamus in Zebrafish? Frontiers in neuroscience 6:64-64.

Mundell NA, Beier KT, Pan YA, Lapan SW, Goz Ayturk D, Berezovskii VK, Wark AR, Drokhlyansky E, Bielecki J, Born RT, Schier AF, Cepko CL (2015) Vesicular stomatitis virus enables gene transfer and transsynaptic tracing in a wide range of organisms. J Comp Neurol 523:1639-1663.

Muto A, Ohkura M, Abe G, Nakai J, Kawakami K (2013) Real-time visualization of neuronal activity during perception. Curr Biol 23:307-311.

Oh SW et al. (2014) A mesoscale connectome of the mouse brain. Nature 508:207-214.

Orger MB, de Polavieja GG (2017) Zebrafish Behavior: Opportunities and Challenges. Annu Rev Neurosci 40:125-147.

Randlett O, Wee CL, Naumann EA, Nnaemeka O, Schoppik D, Fitzgerald JE, Portugues R, Lacoste AM, Riegler C, Engert F, Schier AF (2015) Whole-brain activity mapping onto a zebrafish brain atlas. Nat Methods 12:1039-1046.

Robles E, Laurell E, Baier H (2014) The retinal projectome reveals brain-area-specific visual representations generated by ganglion cell diversity. Curr Biol 24:2085-2096.

Rohlfing T, Maurer CR (2003) Nonrigid image registration in shared-memory multiprocessor environments with application to brains, breasts, and bees. IEEE Transactions on Information Technology in Biomedicine 7:16-25.

Sakai C, Ijaz S, Hoffman EJ (2018) Zebrafish Models of Neurodevelopmental Disorders: Past, Present, and Future. Frontiers in molecular neuroscience 11:294.

Sato T, Hamaoka T, Aizawa H, Hosoya T, Okamoto H (2007) Genetic single-cell mosaic analysis implicates ephrinB2 reverse signaling in projections from the posterior tectum to the hindbrain in zebrafish. J Neurosci 27:5271-5279.

Spickler AR (2016) Vesicular Stomatitis (January, 2016). In. http://www.cfsph.iastate.edu/DiseaseInfo/factsheets.php.

Stuermer CA (1988) Retinotopic organization of the developing retinotectal projection in the zebrafish embryo. J Neurosci 8:4513-4530.

Svara FN, Kornfeld J, Denk W, Bollmann JH (2018) Volume EM Reconstruction of Spinal Cord Reveals Wiring Specificity in Speed-Related Motor Circuits. Cell Rep 23:2942-2954.

Swanson LW, Lichtman JW (2016) From Cajal to Connectome and Beyond. Annual Review of Neuroscience 39:197-216.

Thomas DC, Brewer CB, Roth MG (1993) Vesicular stomatitis virus glycoprotein contains a dominant cytoplasmic basolateral sorting signal critically dependent upon a tyrosine. J Biol Chem 268:3313-3320.

Thyme SB, Pieper LM, Li EH, Pandey S, Wang Y, Morris NS, Sha C, Choi JW, Herrera KJ, Soucy ER, Zimmerman S, Randlett O, Greenwood J, McCarroll SA, Schier AF (2019) Phenotypic Landscape of Schizophrenia-Associated Genes Defines Candidates and Their Shared Functions. Cell 177:478-491 e420.

Vishwanathan A, Daie K, Ramirez AD, Lichtman JW, Aksay ERF, Seung HS (2017) Electron Microscopic Reconstruction of Functionally Identified Cells in a Neural Integrator. Curr Biol 27:2137-2147 e2133.

Wanner AA, Genoud C, Masudi T, Siksou L, Friedrich RW (2016) Dense EM-based reconstruction of the interglomerular projectome in the zebrafish olfactory bulb. Nat Neurosci 19:816-825.

Watabe-Uchida M, Zhu L, Ogawa Sachie K, Vamanrao A, Uchida N (2012) Whole-Brain Mapping of Direct Inputs to Midbrain Dopamine Neurons. Neuron 74:858-873.

Wickersham IR, Sullivan HA, Seung HS (2013) Axonal and subcellular labelling using modified rabies viral vectors. Nature communications 4:2332.

Wickersham IR, Lyon DC, Barnard RJ, Mori T, Finke S, Conzelmann KK, Young JA, Callaway EM (2007) Monosynaptic restriction of transsynaptic tracing from single, genetically targeted neurons. Neuron 53:639-647.

Wilson CA, High SK, McCluskey BM, Amores A, Yan Y-l, Titus TA, Anderson JL, Batzel P, Carvan MJ, Schartl M, Postlethwait JH (2014) Wild Sex in Zebrafish: Loss of the Natural Sex Determinant in Domesticated Strains. Genetics 198:1291.

Yang B, Treweek JB, Kulkarni RP, Deverman BE, Chen CK, Lubeck E, Shah S, Cai L, Gradinaru V (2014) Single-cell phenotyping within transparent intact tissue through whole-body clearing. Cell 158:945-958.

Yee JK, Miyanohara A, LaPorte P, Bouic K, Burns JC, Friedmann T (1994) A general method for the generation of high-titer, pantropic retroviral vectors: highly efficient infection of primary hepatocytes. Proceedings of the National Academy of Sciences 91:9564-9568.

Zhang BB, Yao YY, Zhang HF, Kawakami K, Du JL (2017) Left Habenula Mediates Light-Preference Behavior in Zebrafish via an Asymmetrical Visual Pathway. Neuron 93:914-928 e914.

Zhu P, Narita Y, Bundschuh ST, Fajardo O, Scharer YP, Chattopadhyaya B, Bouldoires EA, Stepien AE, Deisseroth K, Arber S, Sprengel R, Rijli FM, Friedrich RW (2009) Optogenetic Dissection of Neuronal Circuits in Zebrafish using Viral Gene Transfer and the Tet System. Frontiers in neural circuits 3:21.

Zingg B, Chou XL, Zhang ZG, Mesik L, Liang F, Tao HW, Zhang LI (2017) AAV-Mediated Anterograde Transsynaptic Tagging: Mapping Corticocollicular Input-Defined Neural Pathways for Defense Behaviors. Neuron 93:33-47.

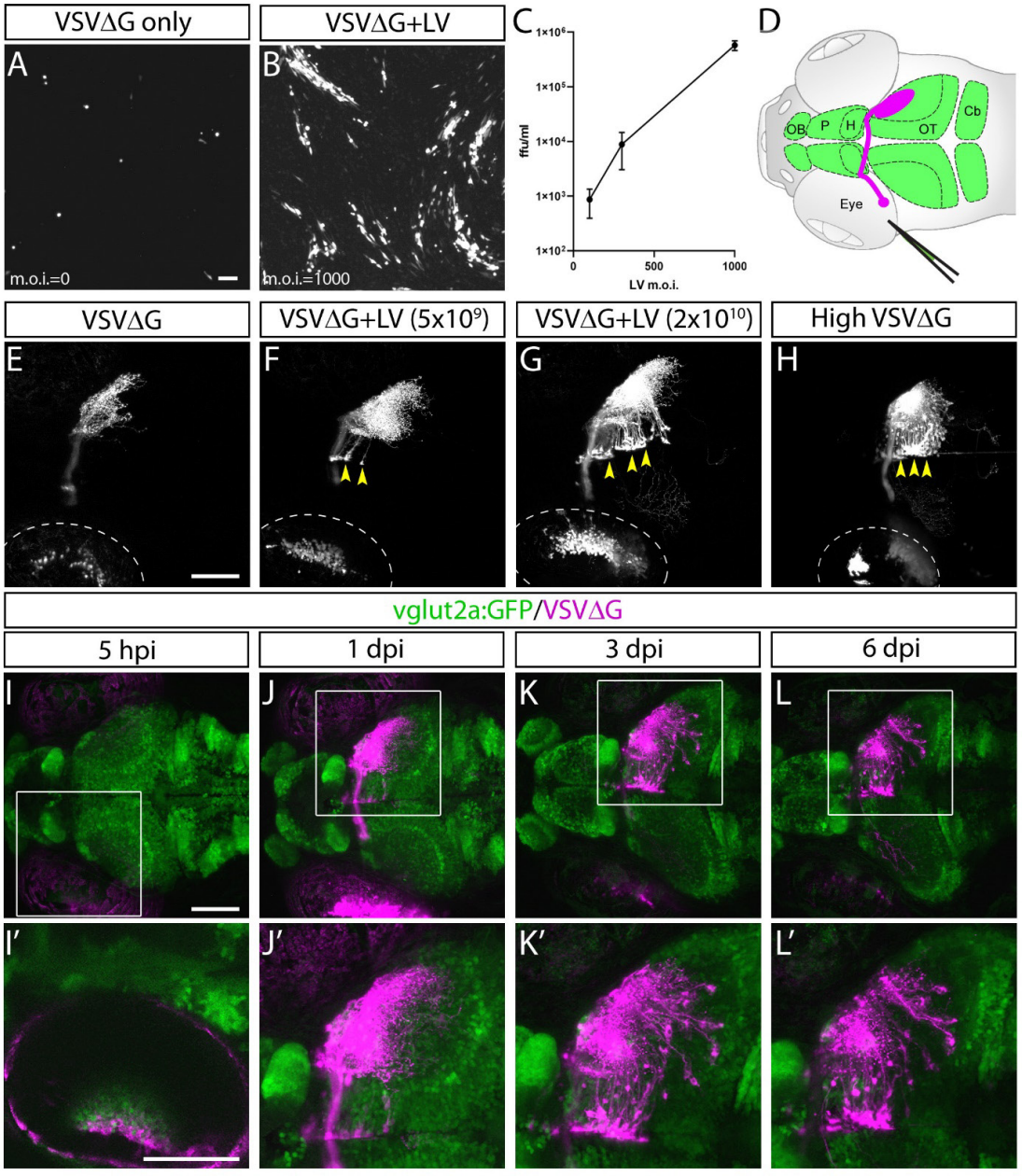
VSVΔG only
VSVΔG+LV
A
B
m.o.i.=0
m.o.i.=1000
C
ffu/ml
LV m.o.i.
D
OB
P
H
OT
Cb
Eye
VSVΔG
VSVΔG+LV (5x10⁹)
VSVΔG+LV (2x10¹⁰)
High VSVΔG
E
F
G
H
vglut2a:GFP/VSVΔG
5 hpi
1 dpi
3 dpi
6 dpi
I
J
K
L
I′
J′
K′
L′

Figure 1

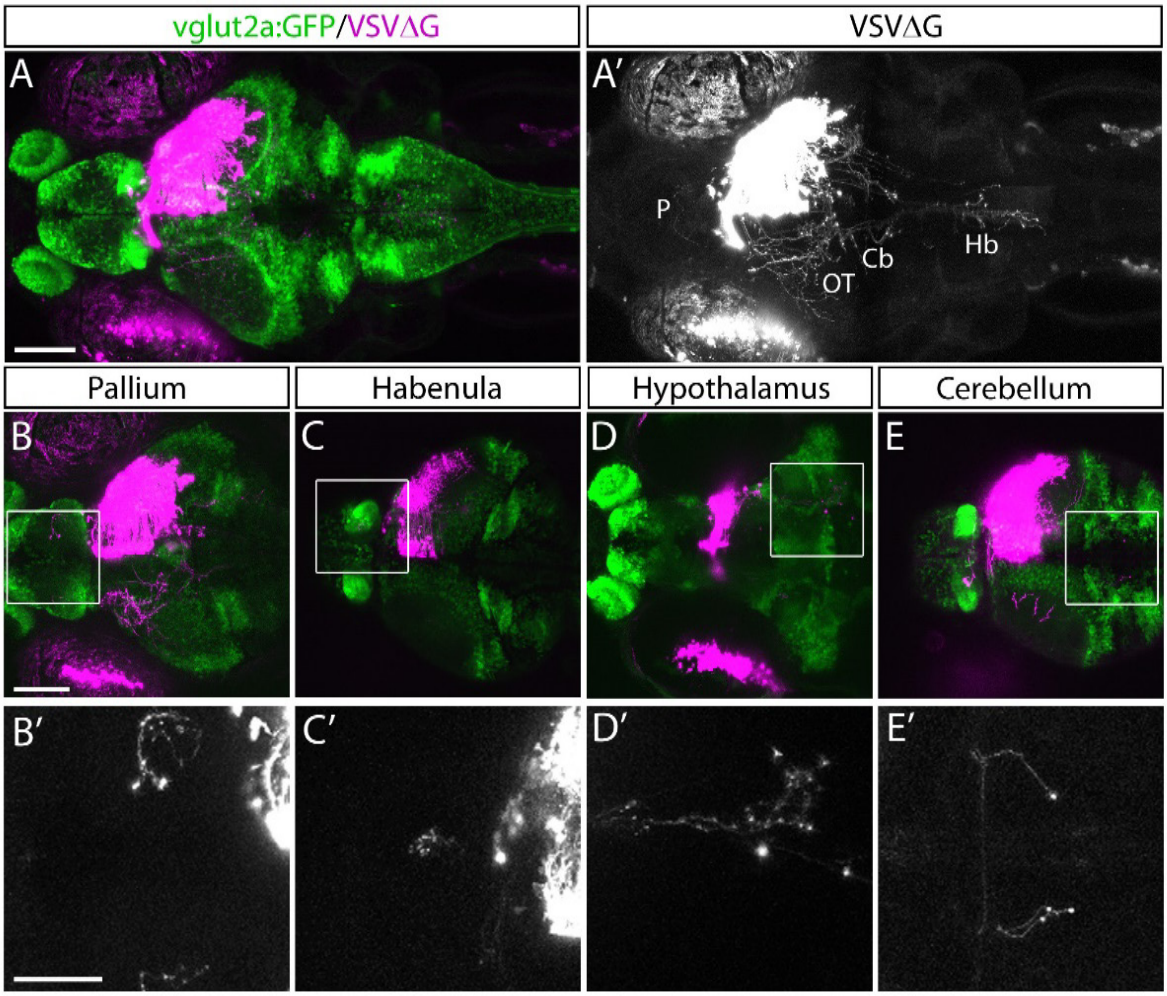
vglut2a:GFP/VSVΔG
VSVΔG
A
A′
P
Cb
OT
Hb
Pallium
Habenula
Hypothalamus
Cerebellum
B
C
D
E
B′
C′
D′
E′

Figure 2

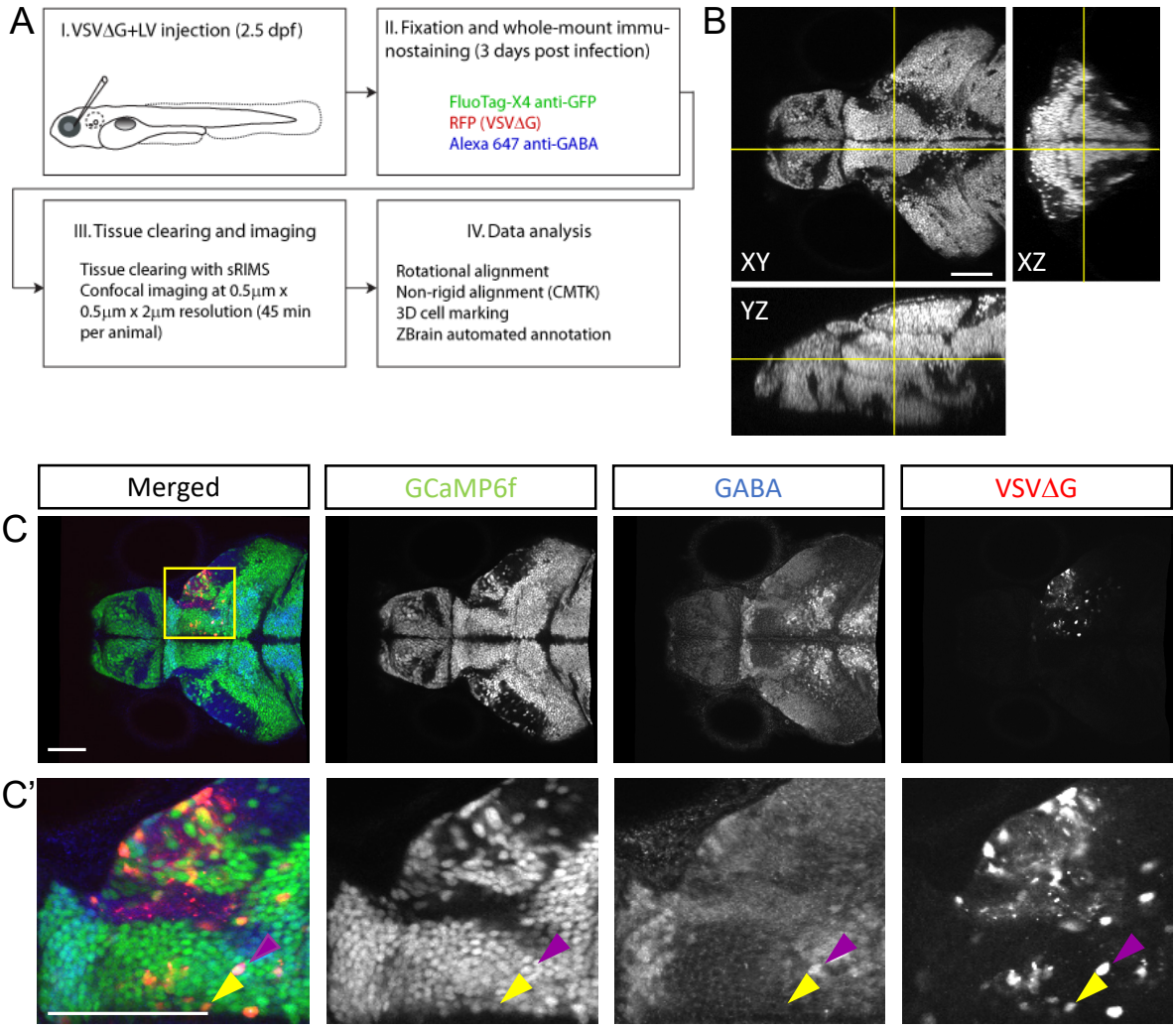
A
I. VSVΔG+LV injection (2.5 dpf)
II. Fixation and whole-mount immu-nostaining (3 days post infection)
FluoTag-X4 anti-GFP
RFP (VSVΔG)
Alexa 647 anti-GABA
III. Tissue clearing and imaging
Tissue clearing with sRIMS
Confocal imaging at 0.5µm x 0.5µm x 2µm resolution (45 min per animal)
IV. Data analysis
Rotational alignment
Non-rigid alignment (CMTK)
3D cell marking
ZBrain automated annotation
B
XY
XZ
YZ
Merged
GCaMP6f
GABA
VSVΔG
C
C'

Figure 3

A

	Wild type (n=24)	*dscaml1-/-* (n=26)
Total TRAS-labeled cells	683 (100%)	671 (100%)
Excitatory	182 (26.65%)	150 (22.35%)
Inhibitory	158 (23.13%)	117 (17.44%)
Non-GCaMP	343 (50.22%)	404 (60.21%)

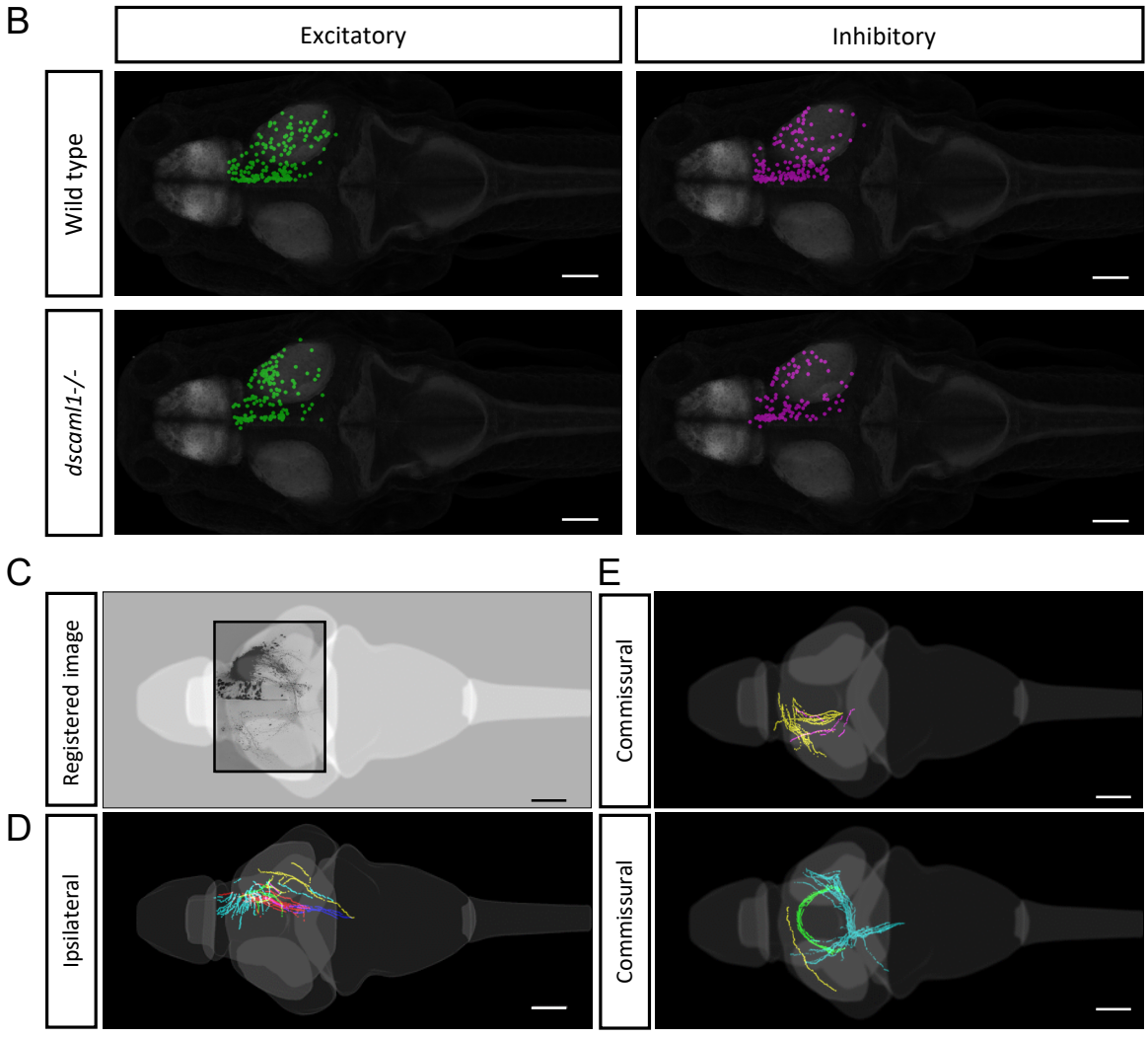

Figure 4

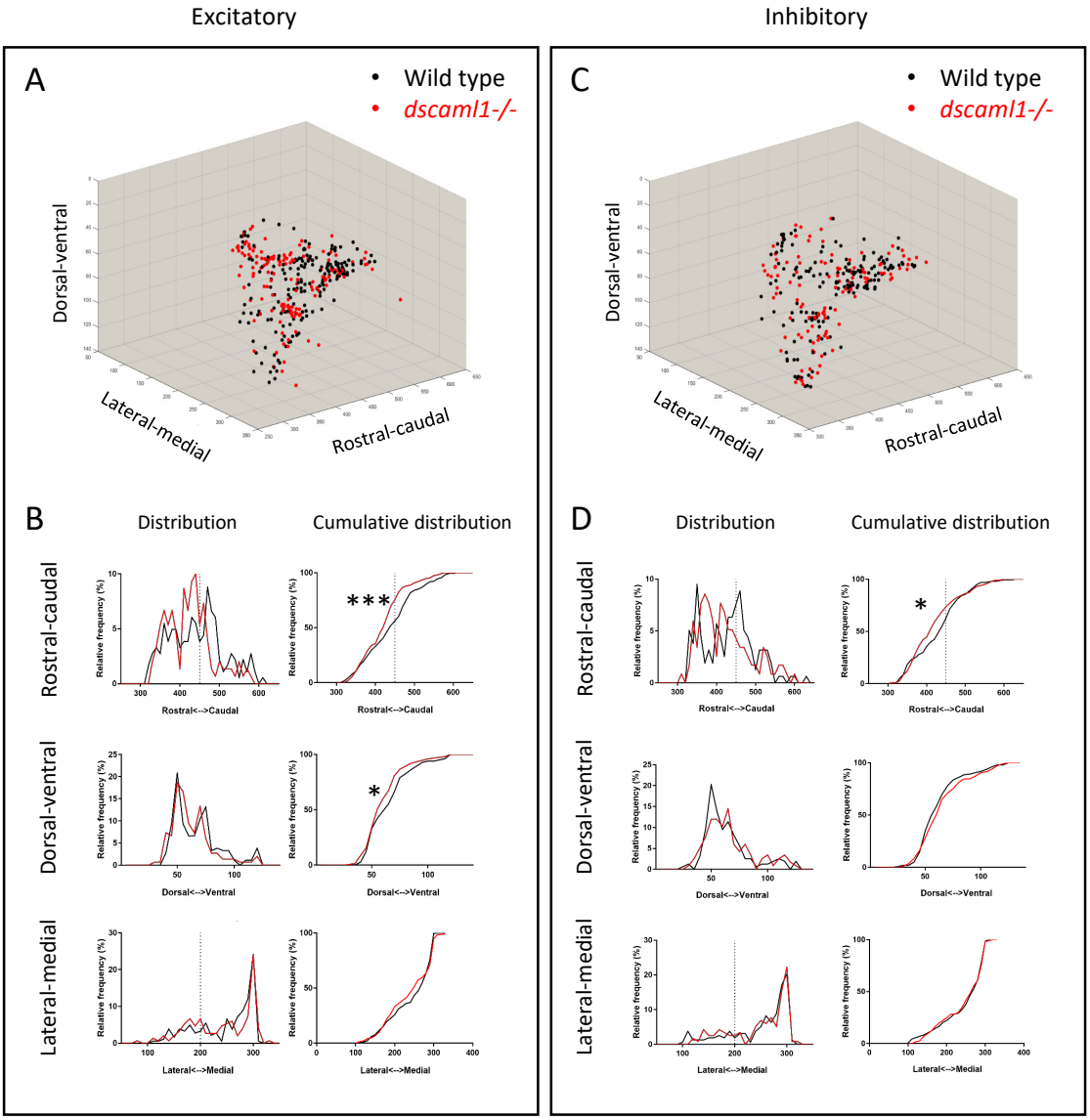
Excitatory
Inhibitory
A
Wild type
dscaml1-/-
Dorsal-ventral
Lateral-medial
Rostral-caudal
C
Wild type
dscaml1-/-
Dorsal-ventral
Lateral-medial
Rostral-caudal
B
Distribution
Cumulative distribution
Rostral-caudal
Dorsal-ventral
Lateral-medial
***
*
*
Relative frequency (%)
Rostral<-->Caudal
Dorsal<-->Ventral
Lateral<-->Medial
D
Distribution
Cumulative distribution
Rostral-caudal
Dorsal-ventral
Lateral-medial
*
Relative frequency (%)
Rostral<-->Caudal
Dorsal<-->Ventral
Lateral<-->Medial

Figure 5

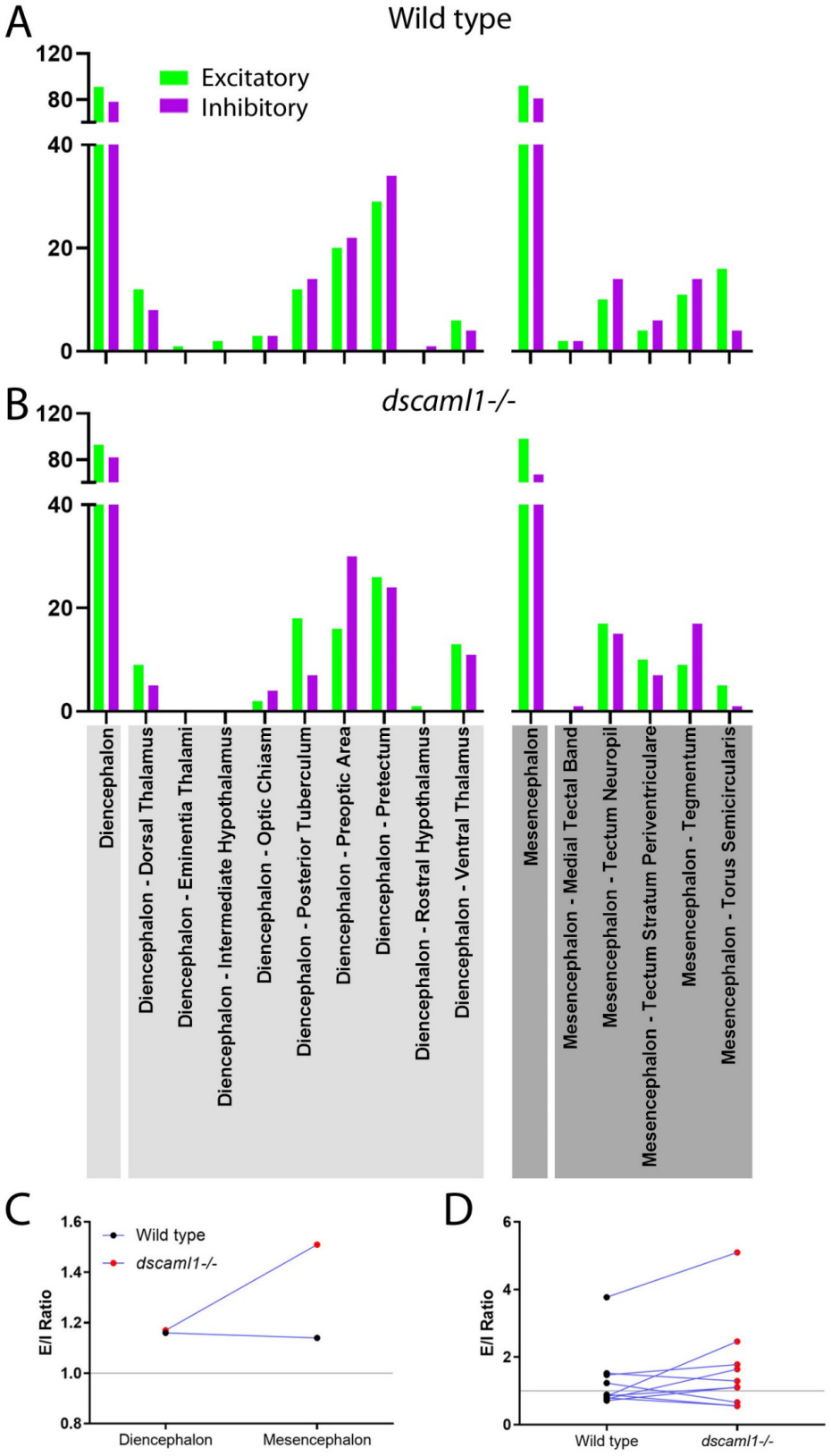
A
Wild type
120
80
40
20
0
Excitatory
Inhibitory
B
dscaml1-/-
120
80
40
20
0
Diencephalon
Diencephalon - Dorsal Thalamus
Diencephalon - Eminentia Thalami
Diencephalon - Intermediate Hypothalamus
Diencephalon - Optic Chiasm
Diencephalon - Posterior Tuberculum
Diencephalon - Preoptic Area
Diencephalon - Pretectum
Diencephalon - Rostral Hypothalamus
Diencephalon - Ventral Thalamus
Mesencephalon
Mesencephalon - Medial Tectal Band
Mesencephalon - Tectum Neuropil
Mesencephalon - Tectum Stratum Periventriculare
Mesencephalon - Tegmentum
Mesencephalon - Torus Semicircularis
C
E/I Ratio
1.6
1.4
1.2
1.0
0.8
Wild type
dscaml1-/-
Diencephalon
Mesencephalon
D
E/I Ratio
6
4
2
0
Wild type
dscaml1-/-

Figure 6

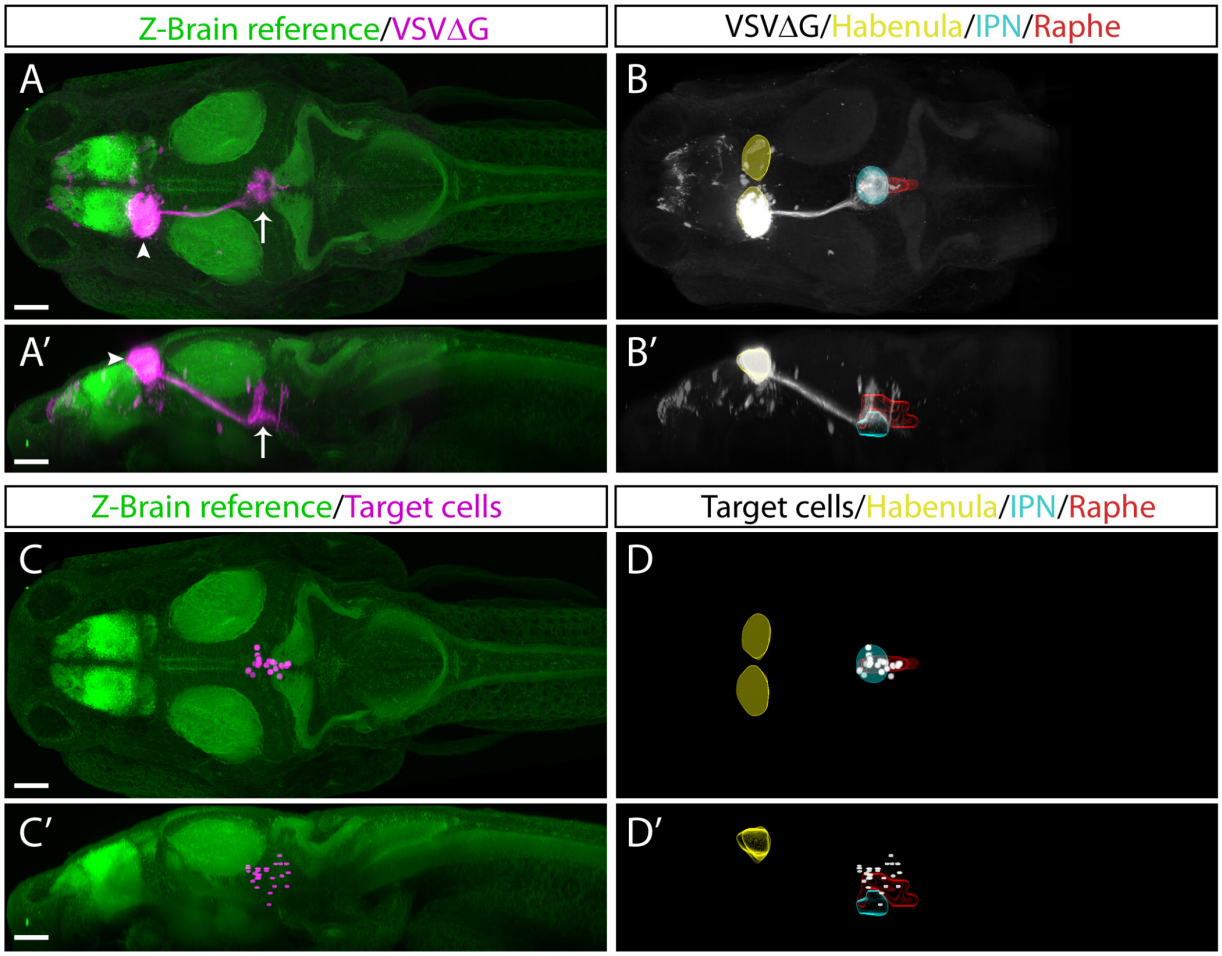
Z-Brain reference/VSVΔG
VSVΔG/Habenula/IPN/Raphe
A
B
A′
B′
Z-Brain reference/Target cells
Target cells/Habenula/IPN/Raphe
C
D
C′
D′

Figure 7

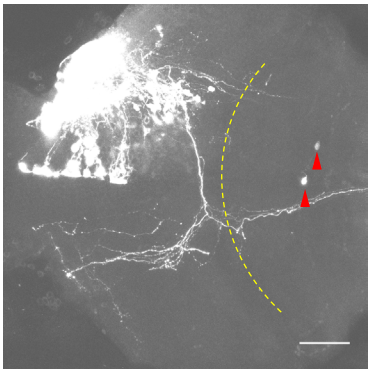

Supplementary Figure S1

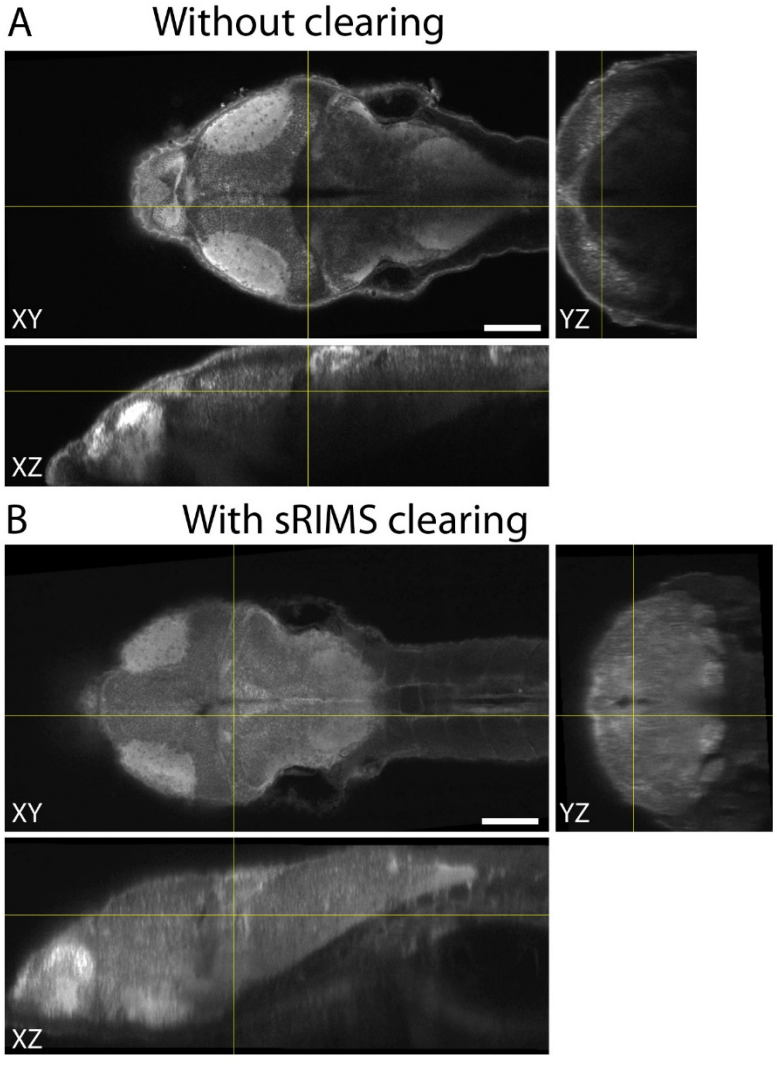

Supplementary Figure S2

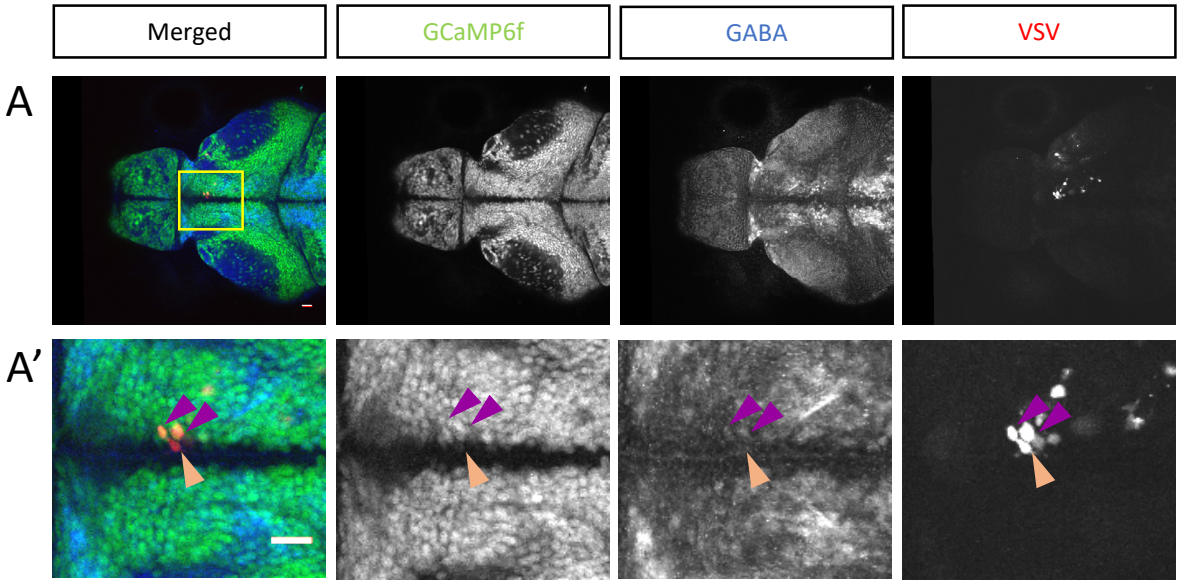

Supplementary Figure S3

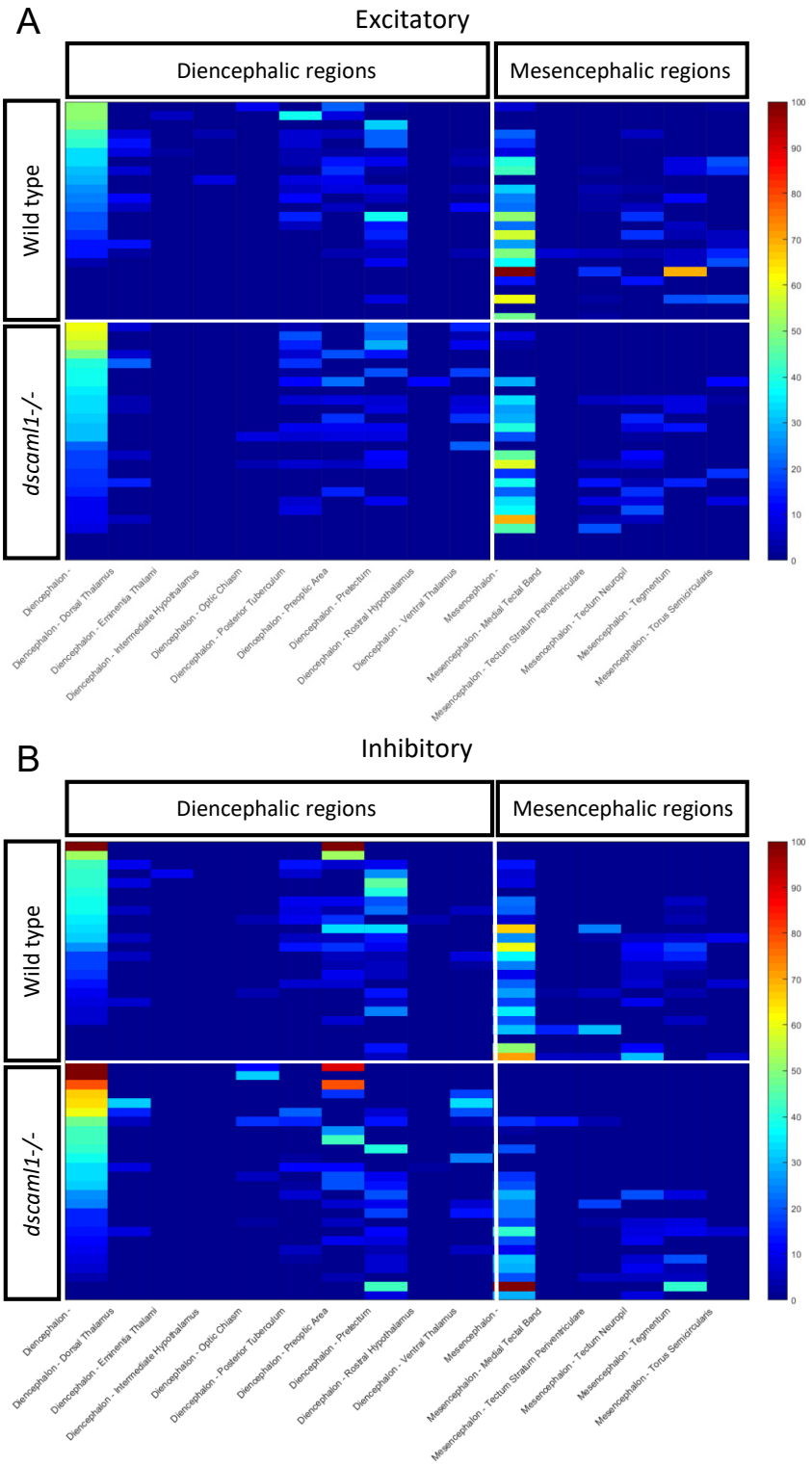

Supplementary Figure S4